Tiago Miguel André Rodrigues

Licenciado em Ciências de Engenharia Mecânica

Wire and arc additive manufacturing: equipment development and parts characterization

Dissertação para obtenção do Grau de Mestre em
Engenharia Mecânica

Orientador: Professora Doutora Rosa Maria Mendes Miranda, Professora Associada com Agregação, aposentada da Faculdade de Ciências e Tecnologia da Universidade Nova de Lisboa

Co-orientador: Mestre Valdemar Rebelo Duarte, Faculdade de Ciências e Tecnologia da Universidade Nova de Lisboa

FACULDADE DE
CIÊNCIAS E TECNOLOGIA
UNIVERSIDADE NOVA DE LISBOA

Julho 2018

Wire and arc additive manufacturing: equipment development and parts characterization

Copyright © 2018 Tiago Miguel André Rodrigues

Faculdade de Ciências e Tecnologia, Universidade Nova de Lisboa

A Faculdade de Ciências e Tecnologia e a Universidade Nova de Lisboa têm o direito, perpétuo e sem limites geográficos, de arquivar e publicar esta dissertação através de exemplares impressos reproduzidos em papel ou de forma digital, ou por qualquer outro meio conhecido ou que venha a ser inventado, e de a divulgar através de repositórios científicos e de admitir a sua cópia e distribuição com objetivos educacionais ou de investigação, não comerciais, desde que seja dado crédito ao autor e editor.

To my grandfather

Acknowledgments

During my academic path I cross myself with people that made me what I am today I helped me to carry out this work, to them my grateful thanks.

First, I would like to express my sincerely thanks to my supervisor, Professor Rosa Miranda, for accepting me to develop a research in this field and for her constant guidance and support along these seven months.

Second, to my co-supervisor, Valdemar Duarte whom always was available to support and advice with my experimental work.

To Professor Telmo Santos for assistance with development the equipment and for providing the infrared thermography camera.

To Professor Jorge Pamies Teixeira and Professor Carla Machado for inviting me to be a monitor of the laboratories of the Mechanical Technology Group of Mechanical and Industrial Engineering Department at Nova University for three consecutive semesters.

To Professor Rui Silva, from CENIMAT I thank for helping with SEM analysis in such a hurry.

To Eng. Marta Freitas, from ISQ for performing the Charpy impact test so promptly.

My sincere gratitude to Mr. António Guinapo Campos and Mr. Paulo M. G. Magalhães for their everyday assistance and friendship.

To my colleagues, David Negrão, Gonçalo Vieira, Henrique Barata and Rui Santos for their companionship throughout these 5 years. Lastly, to my laboratory partners André Silva, Beatriz Crispim, Miguel Machado and Patrick Inácio, my sincerely thanks.

I must express my very profound gratitude to Iana, for her compassion, partnership, loyalty and strength during all these years, she is responsible for my success and one of the most important persons to me. I hope to return such unfailing support throughout my life.

Lastly but not least, to my parents, Rui and Jacinta, for their constant support, kindness, love and for their efforts with providing the best education possible.

Resumo

Wire and arc additive manufacturing (WAAM) é uma tecnologia que compete com as tecnologias de produção aditiva por laser, sendo as maiores vantagens: baixo custo inicial, baixos custos de funcionamento de manutenção, capaz de produzir peças funcionais sem defeitos internos.

Esta tese teve como objetivo de testar e validar um sistema de posicionamento de 3 eixos, produzido no Núcleo de Tecnologia Industrial do Departamento de Engenharia Mecânica e Industrial da Universidade Nova de Lisboa.

As principais características do equipamento são as seguintes: 4.5 m^3 de espaço de trabalho, velocidade de deslocamento máximo no eixo X e Y de 59 mm/s e de 2 mm/s no eixo Z, caracterizado por um desvio posicional máximo de 0.02 mm e uma amplitude de deslocamentos devido às vibrações do equipamento na ordem dos 0.2 mm durante um movimento unidirecional.

O equipamento foi validado produzindo peças em aço de alta resistência com uma fonte de soldadura MIG/MAG, em que foram monitorizados os ciclos térmicos em diferentes camadas através de uma câmera termográfica. As peças fabricadas foram avaliadas pela sua geometria, microestrutura e propriedades mecânicas.

Obtiveram-se peças com bom acabamento superficial tendo sido medida uma ondulação da ordem de grandeza dos 300 μm e sem defeitos internos. Globalmente as peças caracterizaram-se por uma isotropia tanto a nível mecânico como microestrutural. A microestrutura é constituída por ferrite acicular e perlite com durezas inferiores a 320 HV. A espectroscopia por dispersão de energias confirmou que não houve perda dos principais elementos de liga. Os valores da tensão de rotura variaram entre 700 e 809 MPa, dependendo dos processos de processamento. Os ensaios de impacto Charpy em provetes com entalhe em V de dimensões reduzidas registaram valores de energia de absorção de 15 e 18 J nas direções longitudinal (Y) e normal (Z). Observou-se uma superfície de fratura dúctil que também é um indicador relevante do desempenho mecânico das peças produzidas por WAAM.

Palavras-chave

Produção aditiva, WAAM, soldadura, equipamento, aço de alta resistência, microestrutura, propriedades mecânicas

Abstract

Wire and arc additive manufacturing (WAAM) is finding applications in different industrial sectors where it shows to be competitive compared to laser based additive manufacturing technologies. Two major advantages are associated to WAAM: it is a low capital investment technology with reduced running and maintenance costs and allows to manufacture parts with insipient or no porosities.

This study aimed at testing and validating a three-axis positioning system designed and manufactured at Mechanical Technology Group of Mechanical and Industrial Engineering Department at Nova University.

The major characteristics of the developed system are the following: 4.5 m^3 working space, a maximum travel speed of 59 mm/s for the X and Y axes and of 2 mm/s for the Z axis. A maximum positional deviation of 0.02 mm, a minimal travel speed deviation of 0.24 mm/s and a displacement of 0.2 mm of the welding torch due to vibrations during a unidirectional movement.

The equipment was validated by manufacturing thin walls by deposition of a high strength low alloy (HSLA) steel wire with Gas Metal Arc Welding (GMAW), monitoring the thermal cycles by infrared thermography to evaluate them in different layers. Geometrical, microstructural and mechanical characterization of parts was performed.

Manufactured parts exhibited good surface finishing measured by the surface waviness that was around 300 μm and no internal defects were observed. Parts were isotropic as far as microstructural features and mechanical performance are concerned. The microstructure was mainly constituted by acicular ferrite and perlite with hardness below 320 HV. Energy dispersive spectrometry was performed, and no element loss was identified. Ultimate tensile strength varied between 700 and 809 MPa, depending on the process parameters. Resistance to impact was assessed by Charpy V impact tests with reduced size specimens and the absorbed energy registered was of 15 and 18 J, in longitudinal (Y) and normal (Z) directions, respectively. A ductile fracture surface was observed which is also a relevant indicator of mechanical performance of parts produced by WAAM in a HSLA steel.

Key-words

Additive Manufacturing, WAAM, welding, WAAM equipment, HSLA steel, microstructure, mechanical characteristics

Contents

Acknowledgments i
Resumo iii
Palavras-chave iii
Abstract v
Key-words v
Contents vii
List of figures ix
List of tables xiii
Acronyms xv
1 Introduction 1
  1.1 Motivation 1
  1.2 Objectives 2
  1.3 Thesis structure 2
2 Literature Review 3
  2.1 Additive manufacturing 3
  2.2 Additive manufacturing technologies for metal parts 5
    2.2.1 Powder bed fusion 6
    2.2.2 Laser metal deposition 7
    2.2.3 Wire and laser additive manufacturing 7
    2.2.4 Wire and arc additive manufacturing 8
  2.3 Gas metal arc welding 10
  2.4 Recent WAAM developments 12
    2.4.1 Process parameters 13
    2.4.2 Welding shielding gas 14
    2.4.3 Residual stress and distortion 14
    2.4.4 Path planning 16
    2.4.5 Equipment 16
    2.4.6 In-situ monitoring 17
  2.5 Chapter resume and conclusions remarks 17
3 Equipment development and characterization 19
  3.1 Equipment specifications and requirements 19
  3.2 Equipment components 20
  3.3 Characterization techniques 24
    3.3.1 Accuracy tests 24
    3.3.2 Speed tests 27
    3.3.3 Vibration tests 28
  3.4 Chapter resume 29
4 Results and discussion of equipment characterization tests 31

4.1 Accuracy tests results 31
4.2 Speed tests results 38
4.3 Vibration tests results 39
4.4 Chapter resume 40
5 Parts manufactured by WAAM and its characterization 41
5.1 Experimental procedure 41
5.1.1 Material characterization 41
5.1.2 Buildup of samples 42
5.1.3 Infrared thermography 43
5.1.4 Deposition strategy 44
5.1.5 Heat input and deposition rate calculation 45
5.2 Characterization techniques 45
5.2.1 Visual inspection 45
5.2.2 Surface waviness measurement 46
5.2.3 Sample preparation 46
5.2.4 Metallographic analysis 47
5.2.5 Microhardness measurements 47
5.2.6 Uniaxial tensile tests 47
5.2.7 Charpy impact energy test 48
5.2.8 Scanning electron microscopy 48
5.3 Chapter resume 49
6 Results and discussion of manufactured parts and its characterization 51
6.1 Macroscopic characterization 51
6.2 Thermal analysis 53
6.3 Microscopic characterization 58
6.4 Microhardness test results 63
6.5 Uniaxial tensile tests 65
6.6 Fractography 66
6.7 Charpy impact energy test 67
6.8 Energy-dispersive x-ray spectroscopy 68
6.9 Chapter resume 68
7 Conclusions and suggestions for future work 69
References 71

List of figures

Figure 2.1 - Metal additive manufacturing processes [10]. 5
Figure 2.2 - Illustration of a PBF process [11]. 6
Figure 2.3 - Schematic diagram of Laser Metal Deposition [11]. 7
Figure 2.4 - Schematic illustration of a WLAM process [16]. 7
Figure 2.5 - Schematic illustration of WAAM (adapted from [18]). 8
Figure 2.6 - Transfer mode depicted as a function of arc voltage and current intensity (adapted from [45]). 11
Figure 2.7 - Representation of layer thickness and hatch spacing (adapted from [54]). 13
Figure 2.8 - The deterioration of wall quality by increasing TS and maintaining the WFS/TS ratio at 30 m/min [17]. 13
Figure 2.9 - Schematic representation of the shielding device [57]. 14
Figure 2.10 - Schematic diagram of the high-pressure roller [60]. 15
Figure 2.11 - Steps in the hybrid process of metal additive manufacturing combining WAAM and milling [64]. 17
Figure 3.1 - Welding Equipment. 23
Figure 3.2 - Representation of test nr. 1. 24
Figure 3.3 - Representation of test nr. 2. 24
Figure 3.4 - Representation of the test nr. 3. 25
Figure 3.5 - Experimental setup of the two-dial indicator and the Z-height gauge. 25
Figure 3.6 - Representation of the three different paths performed for test nr. 6: a) square, b) zig zag, c) diagonal with circumference. 26
Figure 3.7 - Paths delineated by changing travelling speed during movement for two different paths: a) square, b) diagonal. 26
Figure 3.8 - Test nr. 8 setup. 27
Figure 3.9 - Accelerometer setup. 28
Figure 4.1 - Test nr. 1 results with 100 steps and a micro stepping of 1/1. 31
Figure 4.2 - Test nr. 1 results with 100 steps and a micro stepping of 1/2. 31
Figure 4.3 - Test nr. 1 results with 100 steps and a micro stepping of 1/4. 32
Figure 4.4 - Test nr. 1 results with 100 steps and a micro stepping of 1/8. 32
Figure 4.5 - Test nr. 1 results with 100 steps and a micro stepping of 1/16. 32
Figure 4.6 - Test nr. 2 results with 100 steps and a micro stepping of 1/1. 32
Figure 4.7 - Test nr. 2 results with 200 steps and a micro stepping of 1/2. 32

Figure 4.8 - Test nr. 2 results with 400 steps and a micro stepping of 1/4. 33
Figure 4.9 - Test nr. 2 results with 800 steps and a micro stepping of 1/8. 33
Figure 4.10 - Test nr. 2 results with 1600 steps and a micro stepping of 1/16. 33
Figure 4.11 - Representation of the triangle, hexagon and square dimensions measured. 37
Figure 4.12 - Displacements recorded in the three axes in time domain of run nr.2. 40
Figure 5.1 - LEM LA 200-P current probe. 43
Figure 5.2 - Infrared thermography camera setup on WAAM equipment. 43
Figure 5.3 - Wall appearance without travelling speed control [68]. 44
Figure 5.4 - Deposition strategy of this work single walls. 45
Figure 5.5 - Typical defects that may occur during WAAM depositions: a) Inconsistence wall thickness, b) Variation of final part height and porosity. 46
Figure 5.6 - Surface waviness measurement representation. 46
Figure 5.7 - a) Illustration of the removed sections zones b) Cross sections observed macro and microscopically. 47
Figure 5.8 - Uniaxial tensile test specimen dimensions. 48
Figure 5.9 - Uniaxial tensile tests specimens location. 48
Figure 5.10 - Charpy impact energy test specimens location. 48
Figure 5.11 - EDS analyzed points. 49
Figure 6.1 - Produced parts aspect and corresponding transversal sections of samples: a) P1, b) P2 and c) P3. 52
Figure 6.2 - Schematic illustration of the temperature measurement points. 54
Figure 6.3 - Sequence of thermal cycles on the 4th tracking point of the P3 deposition. 56
Figure 6.4 - Comparison between the HAZ area of samples: a) P2, b) P3. 57
Figure 6.5 - Macrostructure along the height of sample P2 (HAZ: heat affected zone, RZ: re-melted zone). 60
Figure 6.6 - Cross section micrographs of sample P2 in 12 distinct zones (AF: acicular ferrite). 61
Figure 6.7 - Cross section micrographs of sample P3 in 12 distinct zones (AF: acicular ferrite). 62
Figure 6.8 - CCT diagram for a HSLA (A: austenite, PF: polygonal ferrite, WF: Widmanstätten ferrite, GF: granular ferrite, AF: acicular ferrite, and M: martensite) [71]. 63
Figure 6.9 - a) Sample P2 cross section, b) Microhardness profiles for sample P2 along the height, c) Microhardness profiles for sample P2 along the width. 64
Figure 6.10 - a) Sample P3 cross section, b) Microhardness profiles for sample P3 along the height, c) Microhardness profiles for sample P3 along the width. 65
Figure 6.11 - Stress-stain curve of sample P2 in directions: a) longitudinal, b) normal. 66

Figure 6.12 - SEM fractographs of a longitudinal P2 tested specimens in: a) center of fracture b) fracture boundary. 67

List of tables

Table 2.1 - Costs of different parts per manufacturing process [10]. 9
Table 2.2 - Comparison between metal AM technologies. 9
Table 3.1 - Equipment Parameters. 20
Table 3.2- Resolution of X and Y axes linear guides. 22
Table 3.3 - Resolution of Z-axis linear guide. 22
Table 3.4 - Paths delineated on the XY plane. 27
Table 3.5 - Paths delineated on the YZ plane. 28
Table 3.6 - Welding Torch vibration test. 29
Table 4.1 - Test nr. 3 results. 33
Table 4.2 - Measured deviations [mm] after performing a square shape with a = 400 mm. 34
Table 4.3 - Measured deviations [mm] after performing a square shape with a = 250 mm. 34
Table 4.4 - Measured deviations [mm] after performing a square shape with a = 125 mm. 34
Table 4.5 - Measurement deviations [mm] for a zig zag pattern with b = 160 mm and c= 35 mm. 35
Table 4.6 - Measurement deviations [mm] for a zig zag pattern with b = 80 mm and c = 17.5 mm. 35
Table 4.7 - Measurement deviations [mm] for a zig zag pattern with b = 40 mm and c = 8.75 mm. 35
Table 4.8 - Measurement deviations [mm] for the diagonal and circumference geometry with d = 1370 mm and e = 200 mm. 36
Table 4.9 - Measurement deviations [mm] for the diagonal and circumference geometry with d = 685 mm and e = 100 mm. 36
Table 4.10 - Measurement deviations [mm] for the diagonal and circumference geometry with d = 342.5 mm and e = 50 mm. 36
Table 4.11 - Measured deviations [mm] for test nr.7 a) square. 36
Table 4.12 - Measured deviations [mm] for test nr.7 b) diagonal. 37
Table 4.13 - Measurements registered of the triangular shape. 37
Table 4.14 - Measurements registered of the hexagonal shape. 37
Table 4.15 - Measurements registered of the squared shape. 38
Table 4.16 - Speed test results. 39
Table 4.17 - Vibration tests results. 39
Table 5.1 - Chemical composition of the ER110S-G wire electrode [wt.%] [66]. 41
Table 5.2 - Mechanical proprieties of the ER110S-G wire electrode [66]. 42

Table 5.3 - Composition of the welding shielding gases. 42
Table 5.4 - Process parameters of the samples chosen to be reproduced [41]. 42
Table 6.1 - Results of width, height, waviness, deposition rate and heat input for each deposition. 52
Table 6.2 - Comparison between height at arc start and end with the travel speed compensation. 53
Table 6.3 - Cooling rate [Cº/s] of sample P2. 55
Table 6.4 - Cooling rate [Cº/s] of sample P3. 56
Table 6.5 - Residence time [s] between 800ºC and 500ºC. 57
Table 6.6 - Growth of interpass temperature [℃] of P2 and P3 depositions. 58
Table 6.7 - Ultimate tensile strenght and elongation to fracture of the tested specimens. 66
Table 6.8 - Charpy impact test results. 67
Table 6.9 - Chemical composition [wt. %] from EDS test. 68

Acronyms

3D	Three dimensional
AM	Additive Manufacturing
BTF	Buy-To-Fly
CAD	Computed Aided Design
CCT	Continuous Cooling Transformation
CMT	Cold Metal Transfer
CTWD	Contact Tip to Work Distance
EBM	Electron Beam Melting
FGM	Functionally Graded Materials
GFR	Gas Flow Rate
GMAW	Gas Metal Arc Welding
GTAW	Gas Tungsten Arc Welding
HAZ	Heat Affected Zone
HI	Heat Input
HSLA	High Strength Low Alloy
HV	Hardness Vickers
I	Current Intensity
LENS	Laser Engineered Net Shaping
LMD	Laser Metal Deposition
MAG	Metal Active Gas
MIG	Metal Inert Gas
NDE	Non-Destructive Evaluation
NDT	Non-Destructive Testing
PAW	Plasma Arc Welding
PBF	Powder Bed Fusion
RMS	Root Mean Square
RP	Rapid Prototype
RZ	Re-melted Zone
SEM	Scanning Electron Microscope
SLM	Selective Laser Melting
SMA	Shape Memory Alloys
TIG	Tungsten Arc Welding
TS	Travel Speed
UTS	Ultimate Tensile Strength

V	Voltage
WAAM	Wire and Arc Additive Manufacturing
WFS	Wire Feed Speed
WLAM	Wire and Laser Additive Manufacturing
WSG	Welding Shielding Gas

1

Introduction

1.1 Motivation

The 4th industrial revolution, also known as Industry 4.0, is the recent movement towards intelligent automation technology and is encouraging the integration of innovative production systems and advanced information technologies in industry. In this new era, the utilization of modern manufacturing technologies and processes, such as Additive Manufacturing (AM), is crucial due to the need to meet new demands, namely: personalized products, complex parts with tailored mechanical properties and short delivering times [1]. AM experienced a considerable growth over the last years and reports have shown the potential of this technology [2], although there are still some concerns about its performance (technical and economical) and reliability.

Metals are, eventually, one of the most common materials in engineering due to their mechanical characteristics, therefore AM technologies are aiming at being an alternative solution to manufacture metallic parts.

Amongst the technologies used for AM of metallic alloys, those based on laser are the most common, such as selective laser melting and laser metal deposition, but others have been investigated based on electric arc, such as Wire and Arc Additive Manufacturing (WAAM), that shown to be competitive with laser. WAAM requires simple low capital investment costs unlike laser, has high deposition rates and can overcome some of the difficulties associated with processing particular alloys such as those based in Nickel and Titanium and Shape Memory Alloys (SMA) [3], or even high alloy steels prone to cracking phenomena. However, a deeper knowledge of the process is needed in order to enhance surface quality, improve strength and fatigue lifetimes. Additionally, non-destructive testing, standardization and certification of AM parts have to be developed since they are still hindering a wider use of these technologies [4].

1.2 Objectives

This thesis has two major objectives:

1- To characterize a developed three-axis positioning system to produce large and complex-shaped parts by AM with metal inert gas/active gas (MIG/MAG) or tungsten arc welding (TIG). This equipment was developed in the framework of an ongoing PhD thesis, so this work aimed to evaluate the main equipment features, in terms of positioning accuracy, vibration levels, and travel speed ranges. This is important to conclude a relevant piece of equipment with industrial characteristics developed in-house at the Mechanical Technology group.

2- To assess equipment feasibility, by producing thin walls and characterize these in terms of geometrical, microstructural and mechanical aspects. Another purpose is to monitor the temperature cycles experienced by the material during part manufacturing with a thermal data acquisition equipment, in order to correlate the thermal cycles with the microstructure and mechanical proprieties.

1.3 Thesis structure

This thesis is structured in seven chapters.

Chapter 2 provides an overview of the AM state of the art, focusing on wire and arc additive manufacturing process. It highlights relevant findings and breakthroughs reported recently.

Chapter 3 gives a brief description of the equipment developed and its features.

Chapter 4 presents the experimental techniques used to characterize the equipment.

Chapter 5 describes the experimental procedure to manufacture the parts and the techniques adopted for their characterization.

Chapter 6 presents and discusses the results achieved in this study and finally in Chapter 7 the main findings are summarized and specific topics to continue this research are outlined.

2

Literature Review

According to ASTM Standard F2729-12 additive manufacturing is defined as “a process of joining materials to make objects from 3D model data, usually layer upon layer, as opposed to subtractive manufacturing methodologies”. Other synonyms widely used for AM in the literature are rapid manufacturing, additive fabrication, layer manufacturing, direct digital manufacturing, free-form fabrication, amongst others [5].

2.1 Additive manufacturing

During the last few decades, AM has gained interest for design and manufacturing part models and prototypes based on the rapid prototype (RP) concept. Rapid prototyping is often referred as AM, however, some authors [6] remark that the use of this term no longer describes it, since its potentials are being adapted to fabricate functional components in the aerospace, automotive, defense and medical industries [7]. To standardize terminology, ASTM has created various categories where the current AM machine technologies and future ones can be fitted. The seven categories of AM process definition proposed by ASTM are the following:

- **Binder Jetting -** a liquid binding agent is selectively deposited to join powder particles;

- **Direct Energy Deposition -** material is deposited and melted via thermal energy onto a specified surface, where it solidifies;
- **Material Extrusion -** the material is drawn through a nozzle, where it is heated and is then deposited layer by layer;
- **Material Jetting -** a printhead dispenses droplets of a photosensitive material that solidifies under ultraviolet (UV) light;
- **Powder Bed Fusion -** each powder bed layer is selectively fused by using an energy source like laser or electron beam;
- **Sheet Lamination -** sheets or ribbons of metal, are bound together using ultrasonic welding;
- **Photopolymerization -** an ultraviolet (UV) light is used to cure or harden a liquid photopolymer resin, whilst a platform moves the object being made downwards after each new layer is cured.

These groups of processes are capable to produce components with complex shapes that are difficult or impossible to fabricate by the conventional methods such as forging, machining and die casting. These traditional solutions are often impracticable due to the inflexibility of modern designs and the cost associated to produce a die and material wastes. The impact on the development of this manufacturing technology is opening new windows of opportunity for the manufacturing of modern designs and novel materials.

Currently, to answer the demands of the Aerospace industry the focus of AM has shifted to complex-shaped components of Titanium and Nickel alloys. These are used extensively due to high specific strength, thermal and electrochemical compatibility with advanced composite materials [7]. AM has also become a vital element in the concept of the industry 4.0, fundamentally, the idea with this innovative approach is based on the concept of Internet of Things (IoT), it is described as a conception of gathering all the information about production lines, resellers, buyers, products, stock, machines availability and other factors in a big data cloud. Smart factories with IoT implemented will focus on customized demands and AM is the most suitable manufacturing process to promptly obtain parts in a vast range of materials [9]. The overall key benefits and limitations of AM are:

Benefits:

- ✓ Manufacturing of complex parts without the need for molds;
- ✓ Some processes do not require post-process machining;

- ✓ Easy to perform slightly changes in the product design without the need to rearrange the production line or build additional dies;
- ✓ Production of functionally integrated designs in one-step, eliminating the assembly of distinct parts;
- ✓ Less material waste and fewer raw materials required;
- ✓ Small production batches are feasible and economical;
- ✓ Potential for simpler supply chains, shorter lead times and lower inventories.

Limitations:

- Parts size are limited by machines build space;
- Some of AM processes are characterized by low build rates;
- Depending on the process, post surface finishing is sometimes required;
- Missing quality standards;
- Powder based machines are very expensive;
- Intellectual property rights & warranty related limitations.

2.2 Additive manufacturing technologies for metal parts

AM processes for metal components initiate with a feedstock material such as powder or wire and subsequently solidified with the aid of an energy source such as laser, electron beam or electric arc. Figure 2.1 depicts the most widely used AM technologies to produce metallic components.

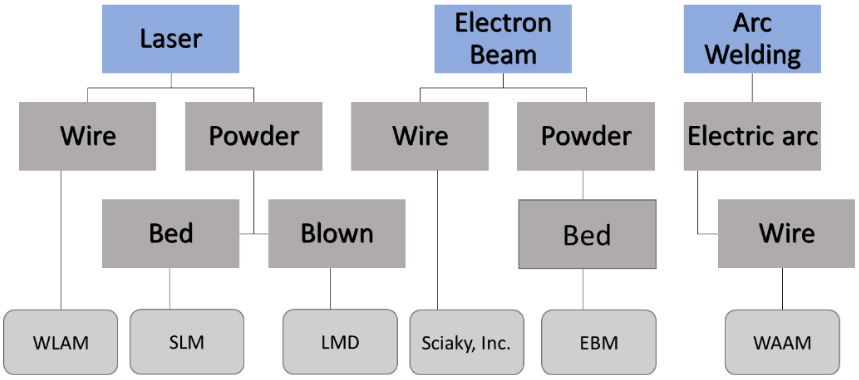

Figure 2.1 - Metal additive manufacturing processes [10].

2.2.1 Powder bed fusion

In general, powder bed fusion (PBF) techniques use a high-density energy beam to melt a thin layer of powder bed. From the 3D CAD, slices of the model are created, and these slices correspond to layers to be melted after the powder is spread by a roller. After finishing one layer, the build platform is lowered by one layer thickness and a new powder bed is spread. This process is repeated until the part is completed. PBF includes all processes where direct energy is used to melt or sinter a layer of a powder bed and it can be done by electron beam or laser. A standard setup of a PBF machine is illustrated in Figure 2.2.

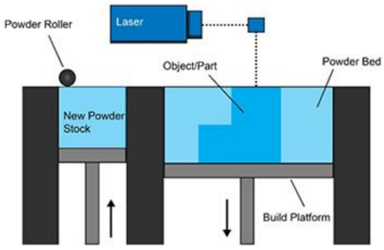

Figure 2.2 - Illustration of a PBF process [11].

Electron Beam Melting (EBM) uses a high-energy electron beam to heat and melt the metal powder by means of the kinetic energy of the electrons which is transferred to the powder particles. To avoid electromagnetic problems, EBM can only process electrically conductive powders and takes place in a vacuum chamber, so that electrons do not interact with the atmosphere and are not reflected.

Selective Laser Melting (SLM) is very similar to EBM but uses a high-power laser that is a coherent light beam where the energy of the photons is absorbed by the powder particles, increasing its temperature above melting temperature. This process takes place in an inert atmosphere to protect the molten metal from oxidation. SLM typically has a system of lenses and a scanning mirror or galvanometer to move the beam.

Powder laser-based technology has been the most popular of AM processes due to its exceptional precision and narrow material waste since the not melted powder can be reused. However, it has some drawbacks related [12] to energy efficiency (in SLM just 10-20% of the total energy input is used to melt the powder). Other common drawbacks [13], includes low deposition rates, high capital cost, availability of consumables, low quality of the metal powder feedstock, a subsequent machining step is often needed, concerns about health and safety risks regarding the powders and it is limited to build low volume parts.

2.2.2 Laser metal deposition

Laser metal deposition (LMD), or laser cladding, is also known as laser engineered net shaping (LENS) [14]. In LMD the powder material is locally supplied by a powder feeding nozzle melts and solidifies in a moving melt pool. LMD is characterized by high efficiency and the flexibility to control the beam position makes it attractive for repairing metallic components. The setup preparation is substantially reduced when compared to SLM. A schematic illustration of the process is presented in Figure 2.3.

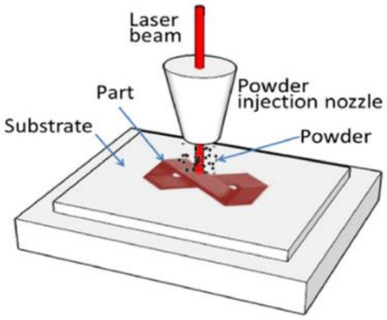

Figure 2.3 - Schematic diagram of Laser Metal Deposition [11].

As an alternative, to high power beams, electric arc is a cheap heat source that can be mastered for producing complex metal parts.

2.2.3 Wire and laser additive manufacturing

Wire and Laser Additive Manufacturing (WLAM) is an AM process that uses wire as feedstock and a laser beam as heat source (Figure 2.4). The equipment consists of an automatic wire-feed system that travels along with the laser and this relative motion is usually performed by a robot, resulting in parts with good surface finishing and with homogeneous properties. WLAM is able to fabricate parts in Titanium and Nickel alloys with good performance. High power fiber lasers have been used for rapid prototyping with direct laser melting of wire [15]. However, this process is difficult to automate, to obtain consistent results and has poor energy efficiency due to the large amount of laser energy that is lost.

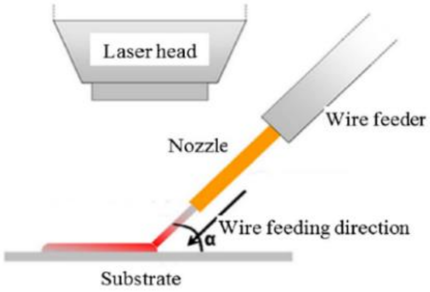

Figure 2.4 - Schematic illustration of a WLAM process [16].

2.2.4 Wire and arc additive manufacturing

Wire and Arc Additive Manufacturing (WAAM) is inserted in the category of Direct Energy Deposition according to ASTM. WAAM (Figure 2.5) is described as the combination of an electric arc as heat source and wire as feedstock to produce large and complex parts [17]. It uses the fundamental concepts of automatized or robotized processes and welding processes, for instance, MIG/MAG, Gas Tungsten Arc Welding (GTAW) or Plasma Arc Welding (PAW).

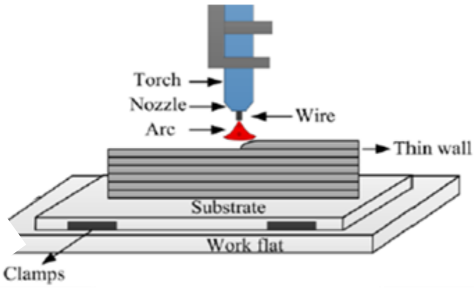

Figure 2.5 - Schematic illustration of WAAM (adapted from [18]).

WAAM relies on welding technologies that are largely mastered which is already an enormous advantage. In fact, WAAM may be capable to overcome other technologies limitations including low costs, because it only requires an axis-robot, a power source, a welding torch, a shielding gas and a substrate. It has high depositions rates in contrast with PBF processes, adequate to fabricate large parts. More, close to zero material waste is obtained if the final part does not need subsequent machining, and it is capable to freeform a large variety of materials.

Thus, the desire to mature this process for its adoption into mass production of aerospace components comes from the ability of producing large parts with a low Buy-To-Fly (BTF) ratio, which is the ratio between the weight of the raw material purchased and the weight of the final part. S.Williams et al. [10] studied the economic benefits of WAAM with subsequent machining and compared to conventional machining from a solid block. The developed model considers the prices of tools, materials, substrate, machine, software, electricity and every consumable for each manufacturing process. Several components were analyzed such as: a wing spar, an external landing gear assembly in titanium and a pylon mount. In all studied cases WAAM represented costs savings compared to conventional machining as shown in Table 2.1**.**

Table 2.1 - Costs of different parts per manufacturing process [10].

Designation	Process	BTF	Cost (€ $\times$ 1000)	Cost Reduction
Wing spar	Traditional	6.5	8.11	n.a.
	WAAM	2.15	5.75	29 %
External landing gear	Traditional	12	18.14	n.a.
	WAAM	2.3	5.6	69 %
Pylon mount	Traditional	5.1	2.8	n.a.
	WAAM	1.5	2.68	7 %

Every process has its capabilities and its field of application so the selection of AM process must be done according to the envisaged application and the avaible equipment.

Table 2.2 presents a summary of studies performed by different research groups and compares different AM processes in terms of surface roughness, layer thickness, deposition rate, dimensional accuracy and materials processed.

Table 2.2 - Comparison between metal AM technologies.

Process	Characteristics					
	Surface Roughness Ra [µm]	Layer Thickness [µm]	Deposition Rate [cm^3/h]	Dimensional Accuracy [mm]	Materials	Refs.
SLM	5-15	20-100	up to 171	0.04-0.2	AISI 420 stainless steel, AISI 4140, AlSi10Mg, Ti-6A-l4V, SS316L, 17-4PH, 15-PH, TA2, TA15,	[19–23]
EBM	10-40	50-200	up to 80	0.04-0.2	Ti-6Al-4V, Inconel 718, SS 316, F75 Cobalt Chromium,	[20,24–28]
LMD	30-60	4-10	up to 300	0.5-1.0	H13 steel, Ti-6Al-4V, IN718, NiTi, Inconel 625	[29–36]
WLAM	8-15	N.A.	up to 250	1.0-1.5	Ti-6Al-4V, Fe-based and Al-based alloys	[15,16,37,38]
WAAM	>200	~900	up to 330	>0.5	Ti-6Al-4V, SS 316, IN 718, H 13 Steel, Fe-based and Al-based alloys, Copper, Nickel aluminum bronze (NAB) alloy, 5A06 aluminium, 5CrNiMo, HSLA steel	[11,17,39–43]

2.3 Gas metal arc welding

Gas Metal Arc Welding (GMAW) also known as Metal Inert Gas (MIG)/Metal Active Gas (MAG), is a gas shielded arc welding process in which an electric arc forms between a consumable electrode wire and the metal workpiece, while the protection of the weld pool is assured by an active or inert gas. GMAW has been a suitable candidate welding process to be adapted for WAAM due to the following key characteristics [44]:

- Easy to use with almost any metallic alloy;
- No welding length restriction;
- High deposition rates and welding speeds;
- Minimal post welding cleaning;
- Easily automated.

In the overall, these characteristics well suit MIG/MAG for a high production additive manufacturing application.

However, GMAW is a rather complex process since several phenomena occur simultaneously and several process parameters must be controlled to avoid slight changes that could drastically influence the quality of the final parts. Process parameters include: wire diameter, wire material, substrate material, preheating substrate, welding equipment, Welding Shielding Gas (WSG), Gas Flow Rate (GFR), voltage (V), current intensity (I), Contact Tip to Work Distance (CTWD), Wire Feed Speed (WFS), Travel Speed (TS) and torch inclination.

There are four major modes of metal transfer in GMAW, though the International Welding Institute has a larger classification. These are: globular, short-circuiting, spray and pulsed-spray, and each one has distinct features (Figure 2.6). The selection of the parameters that directly affect the transfer mode is very important since it affects bead width, penetration, bead size, deposition rate, waviness, heat affected zone (HAZ) and the overall performance of the process. The type of transfer mode is mostly determined by the following main parameters:

- Type of current;
- Electrode diameter and composition;
- Specific power supply characteristics;
- Contact tip to work distance;
- Shielding gas.

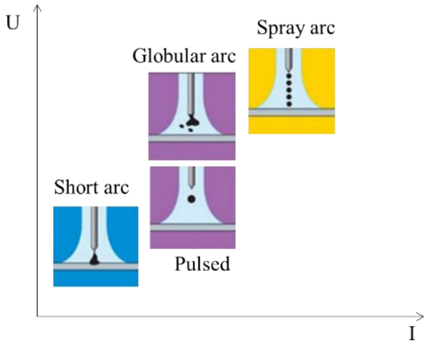

Figure 2.6 - Transfer mode depicted as a function of arc voltage and current intensity (adapted from [45]).

Short circuit transfer occurs for low current intensities and arc voltages decreasing temperature input, minimizing distortion and residual stresses of the final part. Controlled spray transfer is the most used mode in GMAW applications, it avoids the common spray transfer mode problems, such as high heat inputs due to high voltage and current, random droplet size, intensive fumes and spatters. The use of a power source capable to control release of one drop for every sequence of short-circuiting makes this mode very effective.

The welding shielding gas is one of the most influent parameters, since it affects the weld bead geometry, process stability, transfer mode and weld aspect [46]. Shielding gas used are mostly based on Argon and Helium, these inert gases prevent the molten pool from chemically react with the atmosphere and are responsible for conducting electrons between the wire and the substrate. A conductive gas must be ionized and depending on the gas used the ionization energy differs. Ionization potential is defined as the energy necessary to remove an electron from a gas atom generating an ion, or an electrically charged gas atom by removing the valence electrons and is expressed in electron Volt (eV). Argon has an ionization energy of 15.7 eV, while Helium has an energy of 24.5 eV. Due to his low ionization energy, Argon facilitates arc start and provides a more stable arc. The thermal conductivity is a key parameter when selecting a shielding gas, Helium has a high thermal conductivity resulting in more energy being conducted to the workpiece, leading to wider arcs and increased penetration depth. However, adding Helium to an Argon mixture increases thermal conductivity and ionization voltage, which contributes for a more controlled and constant droplet release and deeper beads.

Active gases such as carbon dioxide and oxygen are commonly mixed with inert gases in MAG. Carbon dioxide is a reactive gas common in MAG that allows spray transfer modes and arc stiffness. It allows high travel speeds and deep penetration in ferrous alloys due to exothermic reaction with iron. However, some alloys may form oxides which modify the melting temperature and result in brittle microstructures [47]. The most common gas shield is Argon with 5 or 20% of carbon dioxide, which performs high quality beads, with good arc stability easily ignited. Additions of H_2 are also used , constraining the arc and improving penetration [48]. Mixtures of Argon and Oxygen reduce surface tension, facilitating gases ionization, but they tend to originate porosities.

In the pursuit for a better GMAW based system, a variant of MAG has been adapted in additive manufacturing named Cold Metal Transfer (CMT). It is an advanced transfer process in which an incorporated process-control detects when the electrode wire tip contacts with the molten pool and by activation of a servomotor the wire retracts promoting droplet transfer. Current intensity drops to near-zero and thereby spatter generation is avoided. CMT provides a more stable arc and reduced thermal input due to a slight short-circuit period [49]. This process is suitable for an WAAM application due to effective production costs of high value components for aerospace industry applications, such as Ti-6Al-4V and Inconel 625, consequential of the difficult application of subtractive methods onto these materials.

2.4 Recent WAAM developments

Welding processes can be successfully used in AM, but there is limited research on some of its challenges that are yet to be solved. In particular residual stresses and consequent distortions from excessive heat input, optimization of process parameters and deposition strategy, poor quality of WAAM parts, standardization and difficulties associated with removing finals parts from the substrate.

Wire-feed AM techniques are not recent, their roots go back to 1925, when Ralph Baker patented an invention [50] related the use of an electric arc in producing receptacles or containers of ornamental and useful shapes. By that time, he described temperature distribution and heat transfer problems of this process. Noble [51], in a patent filed in 1919 and assigned to *General Electric Co.*, did the first analysis of cost-effective wire feed arc welding mechanism, describing the process to repair metal shafts. The author pointed out the need for monitoring and the difficult to control process variables to automate the process. Other exciting developments occurred at the beginning of the 70's at *Thyssen-Hütte AG* by using arc welding to produce large shafts and rotors, turbines and electric generators. The author highlights the desire for implementing an automatic online thermal-mechanism to avoid residual stresses and distortion [52]. This "new" fabrication method received considerable interest in the beginning of the 1990's. The disruptive effects of the "new" fabrication approach interested *Rolls-Royce*, that investigated along with Cranfield University its performance to reduce the costs of aero engine components. However, the research failed to consider more parameters such as contact tip to work distance, wire feed speed, wire diameter and fusion characteristics [53].

Difficulties associated with precision, process control and databases for controlling deposition geometry to increase levels of automation, hindered integration of WAAM in industry.

2.4.1 Process parameters

Besides the key process parameters considered in GMAW welding process, for an AM process there are more process parameters that need to be consider, such as, hatch spacing (h_S) and layer thickness (t), both illustrated in Figure 2.7.

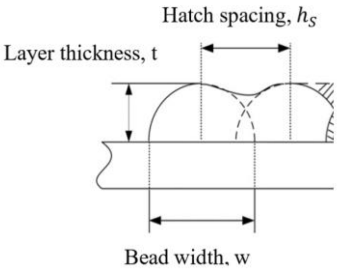

Figure 2.7 - Representation of layer thickness and hatch spacing (adapted from [54]).

Kazanas et al. [17] investigated the production of geometrical features using CMT in which, the low heat input of the process allowed for horizontal walls to be generate from a vertical substrate. A set of experiments varying both the travel and wire feed speeds, maintaining the ratio of WFS/TS, allowed to conclude that TS and WFS are critical regarding wall quality for horizontal walls as illustrated in Figure 2.8.

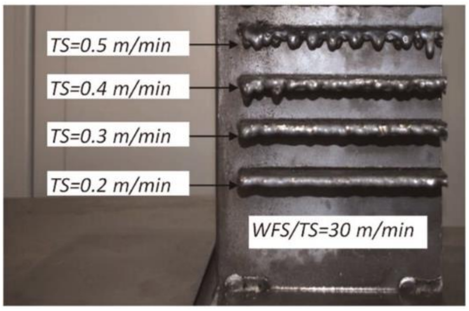

Figure 2.8 - The deterioration of wall quality by increasing TS and maintaining the WFS/TS ratio at 30 m/min [17].

Duarte [41] studied the influence of the five most relevant process parameters (WSG, GFR, WFS, TS and voltage), for both synergic and continuous welding mode, evaluating the width, waviness and deposition rate of the depositions created. The experimental work allowed to conclude that for both synergic pulsed and continuous mode TS and WFS are the most influent parameters on final width. Concerning deposition rate, WFS is the most preponderant parameter for both welding modes. TS is the parameter that most influence the surface waviness in synergic pulsed mode whereas for the continuous mode, the TS and WSG are the most significant ones.

2.4.2 Welding shielding gas

The welding shielding gas is one of the most influent parameters, since it affects bead geometry, process stability, transfer mode and weld appearance [42]. Besides its right selection, other methods have been used to improve WAAM parts quality. Xu et al. [56] studied the effect of oxides on the mechanical proprieties by varying shielding conditions. Results were obtained by making one deposition in open atmosphere with pure argon and the other one in an argon filled tent (chamber), in which the oxygen level was controlled below 300 ppm. Extra tent shielding substantially improved the surface waviness and deposition efficiency by 37% and 9%, respectively.

Gas shielding flow was found to be of remarkably importance regarding walls appearance. In this preliminary study [57] it was analyzed gas shielding flow in WAAM, since turbulence flow causes the shielding gases to mixture with the surrounding air resulting in poor shielding conditions and increased atmosphere contamination that can lead to oxidation. A new device (Figure 2.9) consisted in three distinct parts was created. The first part was a diffusion chamber that uniformly distribute the inlet gas, the second was a honeycomb walls that straightens the flow and reduce its lateral velocities, for last, at the end of the chamber, a layer of metal mesh was used to further improve the uniformity of the flow.

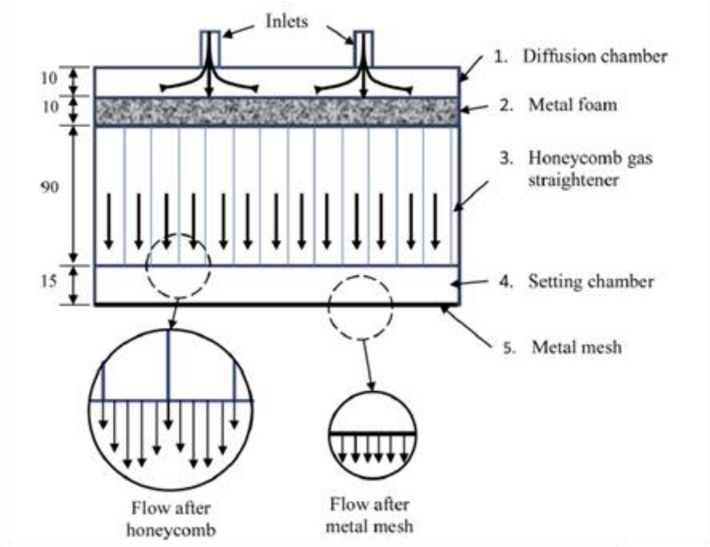

Figure 2.9 - Schematic representation of the shielding device [57].

2.4.3 Residual stress and distortion

During the deposition of layers in WAAM, the process faces complex and large problems of residual stresses and distortions as they are defined as stationary stress at equilibrium in a portion of material [58]. Residual stresses reduce mechanical proprieties of the component and distortion leads to difficulties in achieving the required tolerances. During WAAM process, high temperatures are achieved and will lead to high deformations that after cooling can lead to residual stresses that if these exceed the local yield stress of the material, will lead to plastic deformation, but if it exceeds the ultimate tensile strength will result in fractures.

The material during a deposition undergoes various cycles of expansion and contraction due to the repetitive heating and cooling .There are many techniques that have been study to minimize the effects of residual stresses and distortions in AM. Mughal et al. [59] investigated the effects of process parameters on the residual stress distribution in a GMAW deposition, pointing out the effect that adopting different deposition sequences has on residual stresses distribution, stating that layers starting from outside to the center was the strategy with the lowest impact on the final parts.

The most innovative method yet was made by P. A. Colegrove et al. [60] , in which, an high-pressure rolling was applied in GTAW process to minimize residual stresses. The roller travels horizontally, parallel to the surface, inducing plastic deformation, due to the compression enforced perpendicularly to the substrate (Figure 2.10). The results were very promising, in terms of microstructure, since grain refinement was possible. Furthermore, rolling the sample after every fourth layer had the same effect on the distortion as rolling after each layer but its appliance can be counterproductive, reducing the deposition rate ratio that is one of the major benefits of this process.

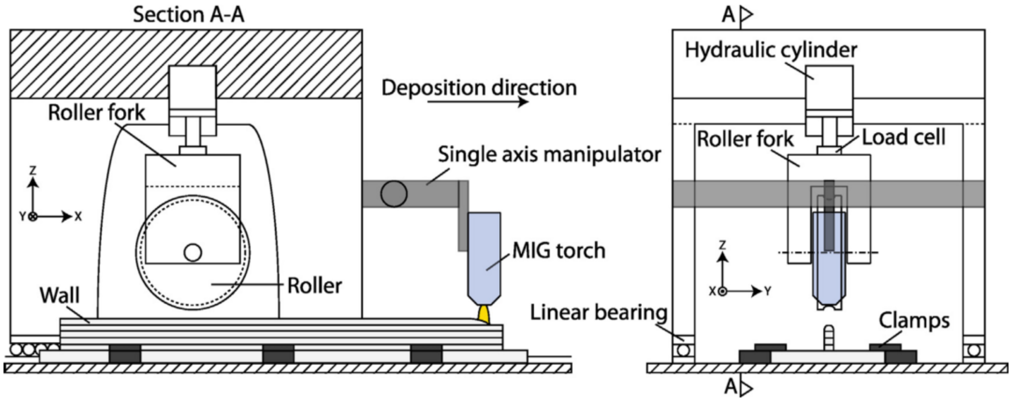

Figure 2.10 - Schematic diagram of the high-pressure roller [60].

Lastly, a suitable solution was validated by means of finite element analysis [61] that considers preheating the substrate. The experimental validation of the walls thermal behavior allowed to conclude that the heat accumulation with preheating results in losses in conductivity, so when layers are deposited, heat losses are minimized resulting in less sharp temperature gradients and, thus, residual stress and distortion can be avoided.

2.4.4 Path planning

Deposition path planning is extremely important not only because it affects residual stress but also the mechanical proprieties of the final part. Poor planning can result in porosity and lack of fusion between adjoining weld beads. D. Ding et al. [62] created an overlapping model to determine the distance between adjacent beads that could suppress the valleys between them. This parameter plays a key role in achieving the required tolerances, geometry accuracy, as well as good surface finish. By approximating beads, the area of the valley automatically decreases, and it is possible to reach an optimized flat surface when the overlapping area equals the valley area. The models of the bead cross-section profile were developed by means of parabola, arc, and cosine functions. This study identified an optimal distance value between adjacent beads of 0.738 times the width of one bead.

It becomes necessary the development of a software able to carry every phenomenon that occurs during deposition to accurately provide the welding torch path, in order to be obtained fully dense and functional parts. Based on the fact that most software for metal deposition are limited and without public access, Yunyong et al. [63] took advantage of the free open source *CuraEngine* introducing new settings to generate G-code to print metallic parts. These settings permit the torch to toggle on and off, path optimization to avoid crossovers in the same layers, the number of start/stop was minimized and an option to pause the torch was also added for subtract cooling between layers. To optimize the wire feed speed, the expected and actual volume of material were calculated, so that they can be matched. The user sets hatch spacing, thickness, wire diameter and the 3D model and *MostMetalCura* would recommend the voltage and wire speed for the process besides generating the G-code to be inserted in a CNC machine.

2.4.5 Equipment

Recently, some machine manufacturers are building optimized machines for the arc welding technology, by integrating additive and subtractive manufacturing technologies into one machine can result in shorter delivery times and personalized complex parts, suppressing WAAM major drawback, which is poor surface finish. Figure 2.11 schematically illustrates the procedure of this hybrid solution.

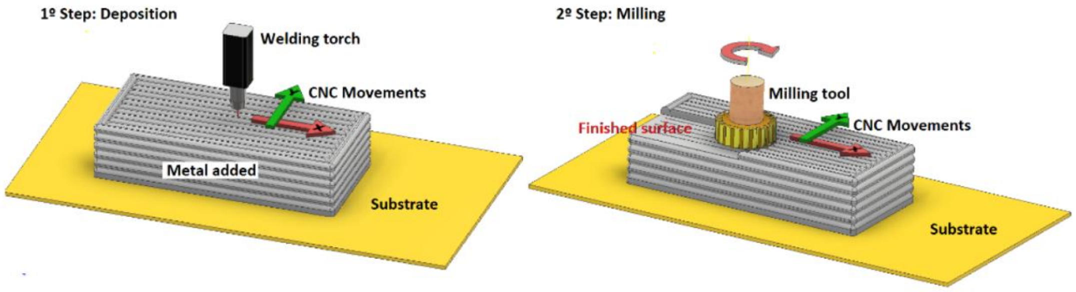

Figure 2.11 - Steps in the hybrid process of metal additive manufacturing combining WAAM and milling [64].

Mazak corporation (Japan) unveiled a machine model VARIAXIS j-600AM featuring a standard WAAM head mounted on the machine headstock as well as an advanced 5-axis multi-surface subtractive capability to produce high-precision parts complete in single setups. Another advancement was made by *Mutoh Industries* that revealed the model Arc MA500-S1 which uses arc welding technologies. However, these machine, are not versatile, since no additional instrumentation or variation of the welding process is possible.

2.4.6 In-situ monitoring

One of the main obstacles of AM is the absence of control and monitoring during the process. Implementation of an in-process monitoring system during the building of a part, will certainly be a step forward in improving the consistency and uniformity across machines, and will allow qualification of AM parts. In the in-situ sensing area, non-destructive evaluation (NDE) sensors can be used to measure and monitor the temperature, the size of the melt pool and the size of beads, and if successfully integrated with a closed loop control system, they might also be able to detect the presence of defects and measure the part dimensions while it is still being produced.

A recent study introduced an innovative closed loop control system integrated in a WAAM equipment [65]. The existence of a dynamic model where the travel speed is selected as the input control variable and the layer width is chosen as the output increased process stability. To support the algorithm, variable like arc current and voltage, heat dissipation, and interpass temperature were evaluated.

2.5 Chapter resume and conclusions remarks

AM processes are now increasingly being used in many applications due to their unique properties. However, improvements are required to fully implement AM in industry. The growing volume of sales of commercial AM equipment and market predictions point towards a deeper market penetration and since large parts are difficult to produce in the commercially available equipment such as PBF ones, the development of a WAAM technology in a fully optimized equipment becomes essential. Although several progressions have been made to overcome WAAM adversities, such as residual stresses, distortions, consistency of mechanical proprieties along a part and defects are still of great concern for companies.

This work aims to contribute for the development of a three-axis positioning system for WAAM at DEMI-FCT NOVA that will further consider the integration of in-process monitoring for defect detection.

At this stage it envisages to validate the equipment developed by processing a High Strength Low Alloy (HSLA) steel and analyzing the parts thermal cycles in order to correlate with the microstructure and mechanical properties obtained.

3

Equipment development and characterization

The first part of this work consisted on final developments, tests and set to work of an equipment to produce large parts by WAAM. The equipment progressed in four stages: a) assembly the mechanical frame, b) design and connect the electric system, c) install the control system and d) testing and validation assessing its effectiveness and repeatability.

3.1 Equipment specifications and requirements

The conception of the following equipment was based on the following functional requirements:

- Human size scale equipment with capability for additional instrumentation to be coupled on the working platform;
- The moving head should be easily adapted for different welding torch types and for other modules to be attached, such as, non-destructive testing (NDT) equipment;
- Independence of the welding torch power and positioning system power supply;
- Welding torch capable to control the WFS separately from the welding machine, process different materials as well as, to deposit more than one material at the same time.

The technical parameters of the machine are given in Table 3.1.

Table 3.1 - Equipment Parameters.

Power	300 W
Overall dimensions [mm]	
Length (X-axis)	2760
Width (Y-axis)	1958
Height (Z-axis)	2000
Working platform size [mm]	
X-axis	2400
Y-axis	1500
Z-axis	1250
Maximum feed rate [mm/s]	
X-axis	59
Y-axis	59
Z-axis	2
Extruders	400
Maximum Acceleration [mm/s^2]	
X-axis	2000
Y-axis	2000
Z-axis	50
Extruders	1000

3.2 Equipment components

Frame: The structure stability was ensured by using 80x80 mm *Bosch Rexroth's* profile that has a high moment of inertia reducing overall deformations without compromise structural integrity. A solid frame that maintains the vibration to an acceptable maximum was essential, since stiffness and versatility are the main characteristics of these profiles, allowing for other machine components to be easily assembled without compromising the strength of the overall structure.

Motion System: The structure comprises a fixed substrate and a travelling head which can move in three orthogonal directions (X, Y, Z) controlled by the seven linear motion guides.

To control the X and Y axis position a *drylin ® ZLW-1040 Standart-02* model was selected, which is characterized by a transmission ratio of 70 mm/rev. This model is driven by a belt which guarantees a maximum deviation of ± 0.2 mm from prescribed position.

For the Z axis, since it has to support the weight of moving parts (welding head, wire feeding system, etc.), four *drylin® SLW-1040* linear guides were preferred, which use a leadscrew to translate the motor rotation into linear motion with a lead of 2 mm. Each linear guide can tolerate an axial load of 700 N.

Stepper motors and drivers: Each linear guide is actuated through stepper motors, the selected model was the *57STH56 NEMA-23 Bipolar* that has an integrated planetary gearbox with a reduction ratio of 4.25/1. These motors were limited to a maximum speed of 375 rev/min, defined by 200 increments per revolution and have a precision of ± 5 %. The assembly was made through shaft couplings to transmit the binary. The motors were controlled by *PiBot Stepper Motor Driver Rev2.2chips* by balancing the power fed into each coil and the driver is also able to sub-divide steps into further increments up to 16 times.

Control Board: This is the most important piece of equipment. The AM machine used an *Arduino Mega 2560* connected to *Ramps 1.4* shield. This module is widely used in 3D printers and it can control the stepper motors up to a 1/16 stepping precision. It is also responsible for the communication with end stoppers, fans, heated bed, with a relay that activates the MIG/MAG welding machine and with the stepper motor attached to the moving head responsible for feeding the wire.

Signal Multiplier: To control the X and Z axis properly the same signal transferred to the X and Z axis in the ramps must be multiplied to every motor of the X-axis and Z-axis move the same distance.

It was essential to calculate this resolution, in order to set in the configurations of the software that will control the machine, to know how many steps the machine should give according to the output required by the G-codes. Equation 3.1 and 3.2 considers the stepper motor steps per revolution, the planetary reduction of the stepper motors gearbox, the mm per revolution transmission of the X and Y linear guides or the screw lead for the Z ones. Additionally, it is necessary to consider the micro stepping selected in the stepper motor driver. Micro stepping is a method of controlling stepper motors, typically used to achieve higher resolution or smoother motion at low speeds.

For the X and Y linear guides comes:

$$\frac{\left[\frac{\text{Steps}}{\text{rev}}\right] \times \text{Gearbox ratio}}{\text{linear guides tansmission } \left[\frac{\text{mm}}{\text{rev}}\right] \times \text{ Microstepping ratio}} = [\text{steps/mm}] \qquad (3.1)$$

Applying equation 3.1 the resolution of the X and Y linear guides is given in Table 3.2.

Table 3.2- Resolution of X and Y axes linear guides.

Micro stepping ratio	[steps/mm]	[mm/steps]
$1/_1$	12,142	0,0824
$1/_2$	24,29	0,0412
$1/_4$	48,57	0,02059
$1/_8$	97,14	0,01029
$1/_{16}$	194,29	0,00515

For the Z linear guides:

$$\frac{\left[\frac{\text{Steps}}{\text{rev}}\right] \times \text{Gearbox ratio}}{\text{Screw lead [mm]} \times \ \text{Microstepping ratio}} = [\text{steps/mm}] \tag{3.2}$$

Making use of equation 3.2 resolution for each micro stepping of the Z-axis linear guides is specified in Table 3.3.

Table 3.3 - Resolution of Z-axis linear guide.

Micro stepping ratio	[Steps/mm]	[mm/steps]
$1/_1$	425	0,00235
$1/_2$	850	0,00117
$1/_4$	1700	0,00058
$1/_8$	3400	0,00029
$1/_{16}$	6800	0,00015

Software: G-code is a programming language to operate the moving head in the three-orthogonal axis to achieve rapid movement, linear interpolation, circular interpolation, amount of material extruded, etc. The equipment was controlled by *Repetier Host* software. This user-friendly program allows to set process variables as the torch travel speed, wire feed speed and the deposition strategy through numerical data using G-code. The code is transferred from the software through a computer port connection into the *Arduino Mega* which reads the inputs and activates each stepper motor without going through each stepper motor driver.

Power supply: A power supply of 12 V and 25 A was installed for electrical support of the full system.

Welding Machine: A welding machine from *KEMPY*, model *Pro MIG 501* (wire feeder and control unit) and model *Pro MIG 3200* (power source), were used to deposit the material over the substrate. This welding equipment (Figure 3.1) allows for three MIG welding options, synergic pulsed wave, synergic continuous wave and conventional continuous wave. In synergic mode the WFS, wire diameter and material were fully selected and the current and the voltage waves were slightly adjusted according to arc height variations. In the conventional wave mode, the user can set the voltage value independently of the WFS value.

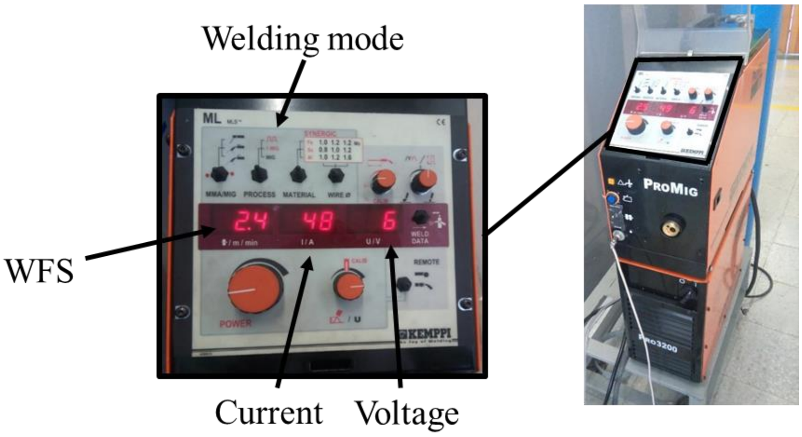

Figure 3.1 - Welding Equipment.

Welding Torch: To increase the freedom in the depositions a customizable torch was developed. It consists simply of a knob gear that clamps and extrudes the wire through the nozzle and of a stepper motor that controls the WFS. To remotely control the torch trigger, the machine was modified by adding an electrical bypass to the torch trigger by a relay, which allowed to turn ON/OFF the torch with a specific command in the G-code. This piece was placed perpendicular to the substrate and allows to control the wire independently, can be used with different wire diameters and materials. The gas flow rate value was controlled by a manometer and the shielding was possible by remotely triggering an electro valve inside the welding machine.

Fume Extractor: A fume extractor *TD MIXVENT* was installed with an extraction capacity of 160 $\mathrm{m^3/h}$ connected to a flexible hose that moves solidary with the welding head to capture harmful gases produced during material depositions.

Emergency button: One emergency red button was installed as specified in the European Standard EN 418 (International Standard: ISO13850) to interrupt the power transmitted to the positioning system and welding machine.

End Stop: At the end of each axis there are limit switches that interrupt movements avoiding crashes of the moving parts.

3.3 Characterization techniques

The equipment developed was tested in order to access: positioning system precision and repeatability, range of travelling speed and vibrations during movements.

3.3.1 Accuracy tests

Before starting with depositions, it was primarily necessary to guarantee repeatability of the deposition conditions with three different test methodologies by assuring consistent quality of the equipment positioning system by quantifying positional errors, straightness errors, squareness errors, circumferential errors. Machine displacement accuracy was measured and quantified individually through *Mitutoyo* dial indicators with a resolution of 0.01 mm.

The first experimental procedure consisted in placing the dial indicator's stylus against a Y-axis linear guide and by moving the X-axis linear guides, as well as to test if the equipment displacement accuracy was affected by number of steps and the micro stepping specified.

For test nr. 1 it was defined 100 steps per mm for each micro stepping and measured the displacement with the dial indicator as illustrated in Figure 3.2. The 300 steps backward and 200 steps forward given in the beginning of each run were necessary to recreate a continue movement, since there is a certain amount of inaccuracy of the positioning system during axis turnaround.

For test nr. 2, theoretical displacement was fixed in 8.235 mm and for each micro stepping the number of steps was varied. (Figure 3.3). Test nr. 1 and nr. 2 were repeated seven times for each micro stepping available.

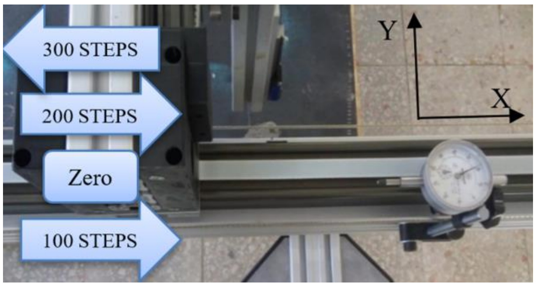

Figure 3.2 - Representation of test nr. 1.

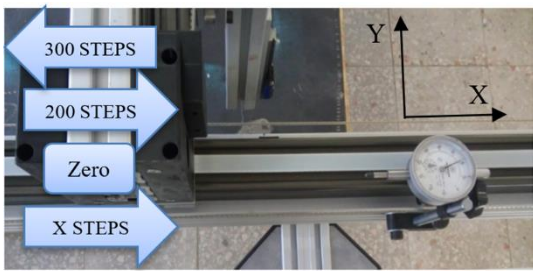

Figure 3.3 - Representation of test nr. 2.

A third test was also carried out to quantify the backlash of the X and Y axis linear guides that occurs during axis turnarounds. Theoretically, the manufacturer set its maximum to 0.2 mm. The experimental procedure consisted in repeating 100 steps backward, 100 steps forward, zeroing the indicator, then performing X steps forward, X steps backward and finally measuring the needle rotations (Figure 3.4). For this test, five different lengths for three different micro stepping ratios were analyzed.

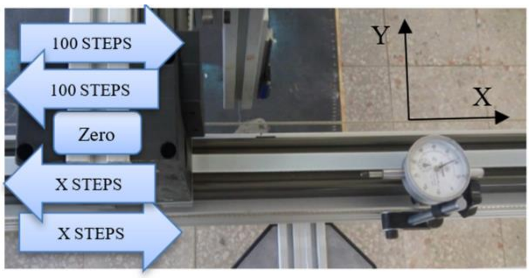

Figure 3.4 - Representation of the test nr. 3.

Moreover, in test nr. 4 it was verified if the backlash was accumulative for a large set of periods of turnarounds by repeating 10 times the number of X steps back and forward of the previously test nr. 3. For this test, five different lengths and three different micro stepping ratios were analyzed.

The second methodology to test equipment accuracy was accessed by using *Repetier Host* software. With this method the three axes were tested as well as bi-directional movements. The experimental procedure consisted in securely mounting the three magnetic bases on the platform and placing the dial indicators stylus and the Z-height gauge against the moving head (Figure 3.5).

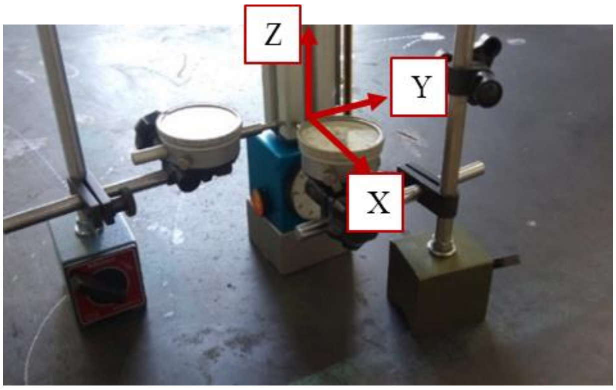

Figure 3.5 - Experimental setup of the two-dial indicator and the Z-height gauge.

To assess Z-axis accuracy a height-gauge with a resolution of 0.01 mm was used. In test nr. 5 by performing upwards and downwards movements with the travelling head.

In test nr. 6 three different paths were delineated making use of G-code. Each test was repeated three times with four different travelling speeds and for three different geometries sizes (Figure 3.6), with a fixed micro stepping of 1/8. Blue rectangle represents the X-axis dial indicator and the orange rectangle the Y-axis. The dimensions “a”, “b”, “c”, “d” and “e” were the variables adjusted for each run.

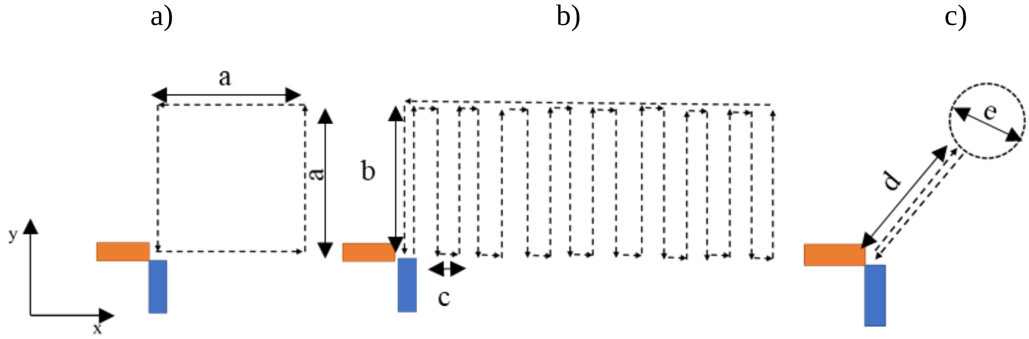

Figure 3.6 - Representation of the three different paths performed for test nr. 6: a) square, b) zig zag, c) diagonal with circumference.

The previous experiments were accomplished by maintaining the travel speed constant during each path. In test nr. 7, was adopted a strategy of varying the travel speed four times during the movement to confirm that a change in speed did not cause the stepper motor to hurdle steps. The first geometry was a square (Figure 3.7a) with speeds of 4.16, 12.5, 25 and 50 mm/s in each square side. The second path was a diagonal (Figure 3.7b) carried out with the same four speeds of the square test. The red lines represent the position of speed modification in each path.

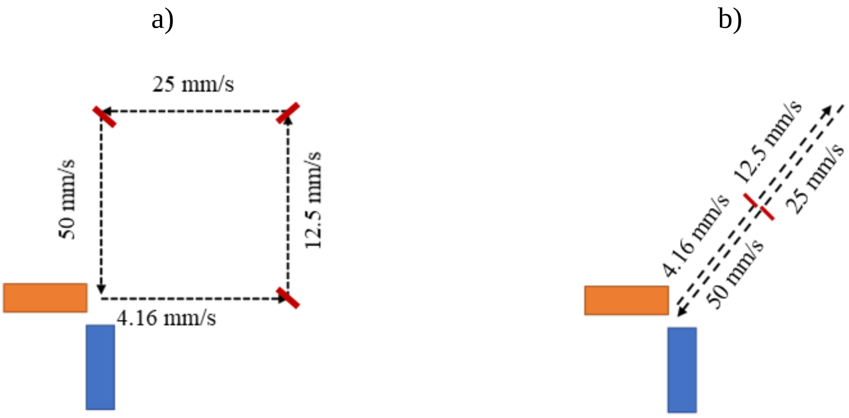

Figure 3.7 - Paths delineated by changing travelling speed during movement for two different paths: a) square, b) diagonal.

The previous methods used G-codes with the relative coordinate system, however it was not sure that the travelling head moved exactly the required distance. For that reason, a third procedure was employed.

In test nr. 8 geometrical features (triangle, square and circumference) were defined, the squareness accuracy was determined by measuring the size of the two diagonals, the perpendicularity of the system by measuring one of the internal angles of the squares. For the circumferential accuracy, the diameter was measured five times along the perimeter. The geometries were drew by assembling a pen in a slide rail that was attached to the moving head and by placing a white paper underneath it. This third methodology for confirming machine accuracy is depicted in Figure 3.8. The measurements were made in the software *Adobe Photoshop CS6*.

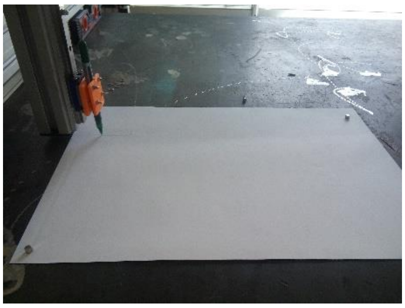

Figure 3.8 - Test nr. 8 setup.

3.3.2 Speed tests

The speed test was conducted by measuring the time span between two defined positions. The differences between the actual speed and the programmed speed were recorded. A chronometer was used with a resolution of 0.01 s. This was performed in sets of three measurements in the same conditions, in different lengths and programmed speeds covering the full range allowed by the equipment. Moreover, three operators were involved in these measurements in order to minimize systematic errors. Eight different runs were tested with only four paths but each one with two different travelling speeds. The three paths defined on the XY plane are illustrated in Table 3.4 and the pathway generated on the YZ plane in Table 3.5. The blue arrows represent the movements performed by the travelling head.

Table 3.4 - Paths delineated on the XY plane.

Run	1 and 2	3 and 4	5 and 6
Plane 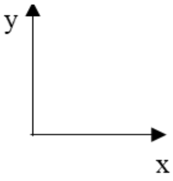 	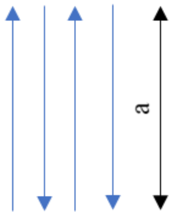 	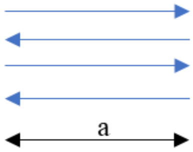 	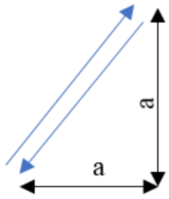

Table 3.5 - Paths delineated on the YZ plane.

Run	7 and 8
Plane 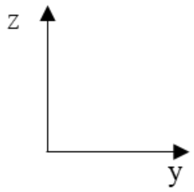	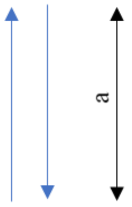

3.3.3 Vibration tests

Displacements of the welding torch during movement was measured with a solid-state MEMS accelerometer *MPU6050*. This device can measure the acceleration in 3 orthogonal directions and has a gyroscope capable to measure yaw, pitch and roll. The digital output of the gyroscope can be tuned to ±250, ±500, ±1000, and ±2000 °/sec and the accelerometer can be set on scales of ±2g, ±4g, ±8g and ±16g.

The accelerometer and the Arduino microcontroller were attached to the welding torch as depicted in Figure 3.9 and data was acquire through a code developed in *Arduino Software (IDE).*

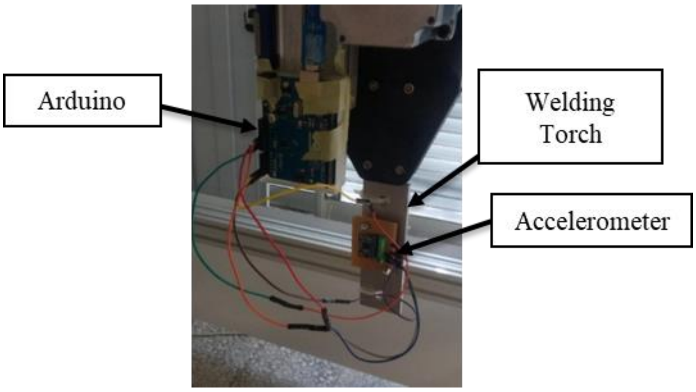

Figure 3.9 - Accelerometer setup.

The time domain is obtained by plotting displacements as a function of time. The sampling data rate was 40 samples per second. The data was plotted after a moving average filter was applied to reduce undesired noise. This type of filtering is acquired by averaging a set of values, always adding a new value to the set and discarding the oldest value. Moreover, to calculate the displacement of the torch, the trapezoidal rule was applied twice, to pass from acceleration to velocity and then to displacement. The overall absolute displacement was calculated by means of equation 3.3.

$$\mathrm{disp}_{abs} = \sqrt{\mathrm{disp}_\mathrm{x}^2 + \mathrm{disp}_\mathrm{y}^2 + \mathrm{disp}_\mathrm{z}^2} \tag{3.3}$$

An interval of the root-mean-square values of the displacements was also given for the time period considered.

Tests performed to analyze displacements resultant of vibrations are specified in Table 3.6. Run nr.1 and nr.2 were made by moving the torch on the X-axis with a travelling speed of 25 mm/s and 50 mm/s respectively. Run nr.3 and nr.4 were conducted by making the torch performed a unidirectional movement on the Y-axis, here it was also experienced with the previous two different TS. Run nr.5 was made on the Z-axis with a travelling speed of 0.75 mm/s and run nr.6 as well on the Z-axis with a travelling speed of 2 mm/s. Finally run nr.7 was made to verify the displacement during a bi-directional movement on the XY plane with both motors running at 50 mm/s. During the trials, the extruder motor was also running to reproduce working conditions.

Table 3.6 - Welding Torch vibration test.

Run nr.	**Travelling speed [mm/s]**	**Distance travelled [mm]**	**Axis tested**
1	25	500	X
2	50	1000	X
3	25	500	Y
4	50	1000	Y
5	0.75	20	Z
6	2	20	Z
7	50	1000	X and Y

3.4 Chapter resume

This chapter describes the functional requirements of the developed equipment as well as its features. Moreover, it presents the experimental tests performed to evaluate the equipment, regarding speed, vibration and accuracy of the positioning system.

4

Results and discussion of equipment characterization tests

4.1 Accuracy tests results

The theoretical values were calculate based on the number of steps/mm for the X and Y axis linear guide previously presented in Table 3.2. Test nr. 1 results are given from Figure 4.1 to Figure 4.5.

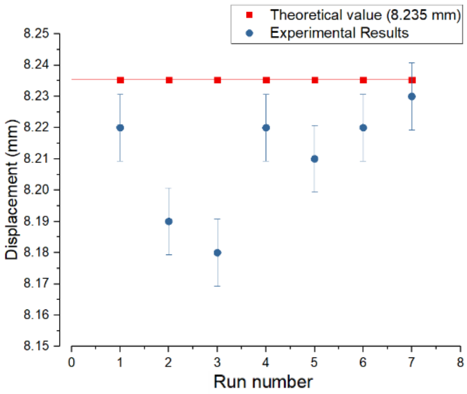

Figure 4.1 - Test nr. 1 results with 100 steps and a micro stepping of 1/1.

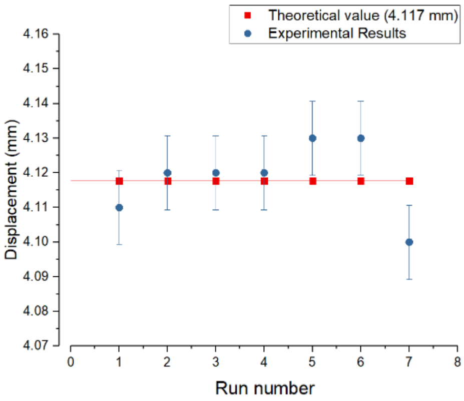

Figure 4.2 - Test nr. 1 results with 100 steps and a micro stepping of 1/2.

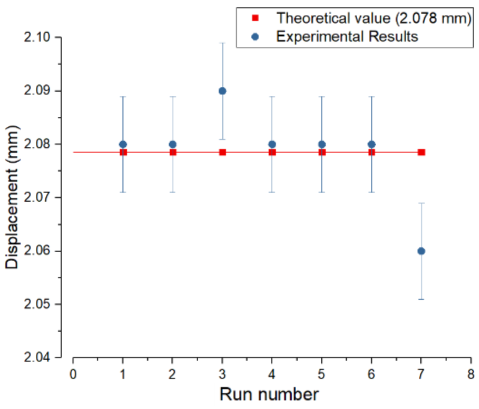

Figure 4.3 - Test nr. 1 results with 100 steps and a micro stepping of 1/4.

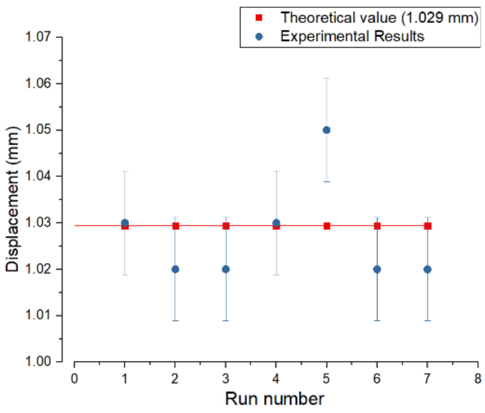

Figure 4.4 - Test nr. 1 results with 100 steps and a micro stepping of 1/8.

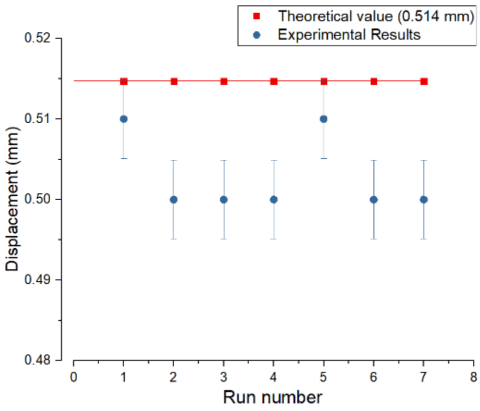

Figure 4.5 - Test nr. 1 results with 100 steps and a micro stepping of 1/16.

Observing test nr. 1 results it can be seen that experimental measured values fit quite well for ratios of 1/2 and 1/4 while they show deviations for other ratios. These deviations can be explained by the difficulties encountered to align perfectly the X-axis with the dial indicator. The maximum inaccuracy measured was of 0.055 mm for a micro stepping ratio of 1/1.

Test nr. 2 results are depicted from Figure 4.6 to Figure 4.10.

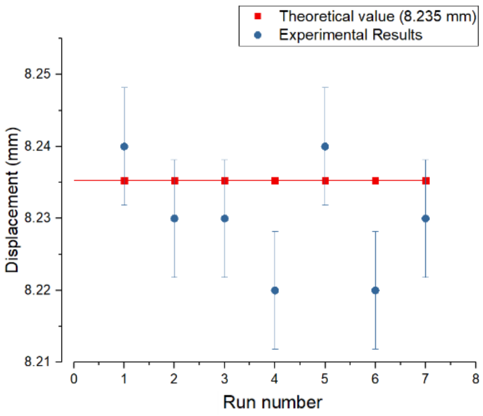

Figure 4.6 - Test nr. 2 results with 100 steps and a micro stepping of 1/1.

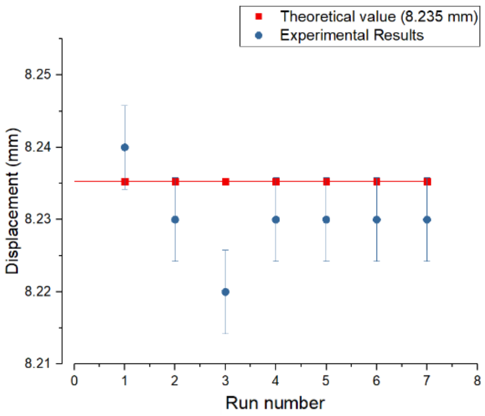

Figure 4.7 - Test nr. 2 results with 200 steps and a micro stepping of 1/2.

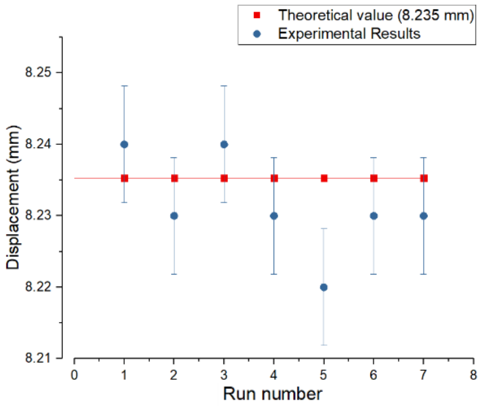

Figure 4.8 - Test nr. 2 results with 400 steps and a micro stepping of 1/4.

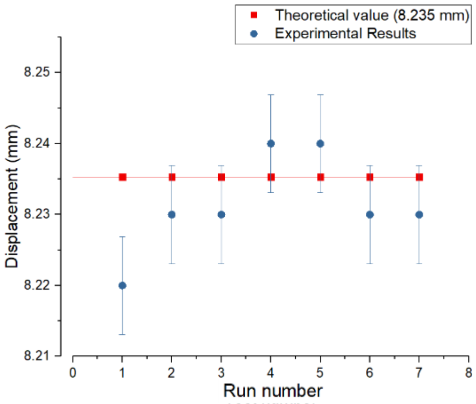

Figure 4.9 - Test nr. 2 results with 800 steps and a micro stepping of 1/8.

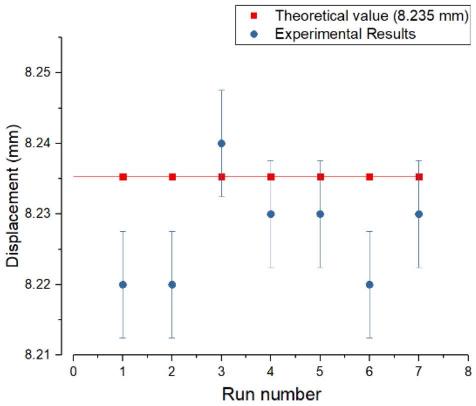

Figure 4.10 - Test nr. 2 results with 1600 steps and a micro stepping of 1/16.

The maximum inaccuracy measured was of 0.015 mm, obtained in at least one run of every micro stepping ratio tested. This confirms that the machine accuracy is not affected by different micro stepping ratios.

Test nr. 3 results of the backlash quantification for different distance travelled and micro stepping ratios are given in Table 4.1.

Table 4.1 - Test nr. 3 results.

Test number	Total distance travelled [mm]	Backlash quantification [mm] for a micro stepping of:		
		1:2	1:4	1:8
1	823.53	0.17	0.15	0.17
2	82.35	0.15	0.15	0.15
3	41.18	0.14	0.15	0.16
4	20.59	0.15	0.16	0.16
5	8.24	0.15	0.14	0.16

Analyzing Table 4.1 it can be seen that the backlash is always below ± 0.2 mm, which was the value defined for the linear guides by the manufacturer. Additionally, it is not influenced by different lengths travelled or micro stepping ratios tested.

In every nr. 4 test runs the dial indicator returned to zero, which means the backlash was not incremental.

Regarding test nr. 5, used to check Z-axis accuracy, three different speeds (0.25 mm/s, 0.75 mm/s and 1.5 mm/s) for two different distance travelled (20 mm and 200 mm) were tested. After one axis reversal at every run the needle returned to the starting point. This result was expected due to the high resolution of the Z-axis linear guides previously shown in 3.2.

Test nr. 6 results are given from Table 4.2 to Table 4.10. The results for the three squares with a side of 400, 250 and 125 mm are respectively showed in Table 4.2,Table 4.3 and Table 4.4. A plus signal means that the travelling head course was more than expected, in contrast to a minus signal that means that a part of course was not fulfilled.

Table 4.2 - Measured deviations [mm] after performing a square shape with a = 400 mm.

Travelling Speed [mm/s]		**4.16**		**12.5**		**25**		**50**	
Axis		X	Y	X	Y	X	Y	X	Y
Run nr.	1	0	0	0	0	0.02	0	0	0
	2	0	0	0	0	0	0	0	-0.01
	3	0	0	0	0	0	0	0	0

Table 4.3 - Measured deviations [mm] after performing a square shape with a = 250 mm.

Travelling Speed [mm/s]		**4.16**		**12.5**		**25**		**50**	
Axis		X	Y	X	Y	X	Y	X	Y
Run nr.	1	-0.01	0	0	0	0	0	0.01	0
	2	0	-0.01	0	-0.01	0	0	-0.01	0
	3	0	0	0	0	0	0	-0.01	-0.02

Table 4.4 - Measured deviations [mm] after performing a square shape with a = 125 mm.

Travelling Speed [mm/s]		**4.16**		**12.5**		**25**		**50**	
Axis		X	Y	X	Y	X	Y	X	Y
Run nr.	1	0	-0.01	0	0	0	0	0	0
	2	0	0	0	0	0	0	0	0
	3	0	0	0	0	-0.01	-0.02	0	0

Analyzing the results, it can be concluded that for this geometry, when X and Y linear guides are moving independently, both travel speed and time travelled do not affect the accuracy. The highest measured value was of 0.02 mm.

From Table 4.5 to Table 4.7 it is presented the results for the zig zag pattern.

Table 4.5 - Measurement deviations [mm] for a zig zag pattern with b = 160 mm and c= 35 mm.

Travelling Speed [mm/s]		**4.16**		**12.5**		**25**		**50**	
Axis		X	Y	X	Y	X	Y	X	Y
Run nr.	1	0	0	0.02	0.01	0	0	0.01	0
	2	0	0	0	0	0	0	0	0
	3	-0.02	-0.01	0	0	0	-0.01	0	0

Table 4.6 - Measurement deviations [mm] for a zig zag pattern with b = 80 mm and c = 17.5 mm.

Travelling Speed [mm/s]		**4.16**		**12.5**		**25**		**50**	
Axis		X	Y	X	Y	X	Y	X	Y
Run nr.	1	0	0	-0.02	0	0	0	0	0
	2	0	0.01	0	-0.01	0	0	0	0
	3	0	0	0	0	0	0	0	0

Table 4.7 - Measurement deviations [mm] for a zig zag pattern with b = 40 mm and c = 8.75 mm.

Travelling Speed [mm/s]		**4.16**		**12.5**		**25**		**50**	
Axis		X	Y	X	Y	X	Y	X	Y
Run nr.	1	0	0	0	0	0	0	-0.01	0
	2	0	0	0	0	0	0	0	-0.01
	3	-0.01	0	0	0	0	0	0	0

For this configuration the system demonstrated to be very accurate, since the end point was almost the same as the start one and the deviations are below 0.02 mm which is reasonable for this equipment, since commercial fused filament fabrication 3D printers have accuracies around 0.2 mm. The analysis of the error leads to the conclusion that the test of unidirectional and repetitive turnarounds does not represent any trend with increasing the length or the travel speed.

The third geometry was necessary to test a bidirectional movement. The accuracy results for are given in Table 4.8,Table 4.9 and Table 4.10.

Table 4.8 - Measurement deviations [mm] for the diagonal and circumference geometry with d = 1370 mm and e = 200 mm.

Travelling Speed [mm/s]		**4.16**		**12.5**		**25**		**50**	
Axis		X	Y	X	Y	X	Y	X	Y
Run nr.	1	0	0	0	0	0	0	0.01	0
	2	0	0	-0.01	0	-0.01	0	0	0
	3	-0.02	0	0	0	0	0	0	0

Table 4.9 - Measurement deviations [mm] for the diagonal and circumference geometry with d = 685 mm and e = 100 mm.

Travelling Speed [mm/s]		**4.16**		**12.5**		**25**		**50**	
Axis		X	Y	X	Y	X	Y	X	Y
Run nr.	1	0	0	-0.01	0	0	0	0	0
	2	0	-0.01	0	0	0	0	0	0
	3	0	0	0	0	0	0	0	0

Table 4.10 - Measurement deviations [mm] for the diagonal and circumference geometry with d = 342.5 mm and e = 50 mm.

Travelling Speed [mm/s]		**4.16**		**12.5**		**25**		**50**	
Axis		X	Y	X	Y	X	Y	X	Y
Run nr.	1	0	0	-0.02	0	0.01	0.02	0	0.01
	2	0	0	0	-0.01	0	0	0	0
	3	0	0	0	0	0	0	0	0

As expected, analyzing Table 4.8,Table 4.9 and Table 4.10 the values measured are under 0.02 mm for bi-directional accuracy test. The analysis of the error leads to the conclusion that performing bi-directional movements and circumferences do not affect equipment accuracy.

The results of test nr.7 in which the travelling speed was varied during movement when performing a square (a) and a bi-directional movement (b) are presented in Table 4.11 and Table 4.12, respectively.

Table 4.11 - Measured deviations [mm] for test nr.7 a) square.

Run nr.	**Axis**	
	X	**Y**
1	0	0
2	0	0
3	0	0

Table 4.12 - Measured deviations [mm] for test nr.7 b) diagonal.

Run nr.	Axis	
	X	**Y**
1	0.01	0
2	0	0
3	0	0

It was verified that changing travelling speed during movements did not interfered with accuracy.

In test nr.8, a pen was fixed on the moving head and a set of simple geometries with different sizes were drew. Results are shown in Table 4.13,Table 4.14 and in Table 4.15 for a triangle, hexagon and square geometries respectively, with the measured dimensions depicted in Figure 4.11.

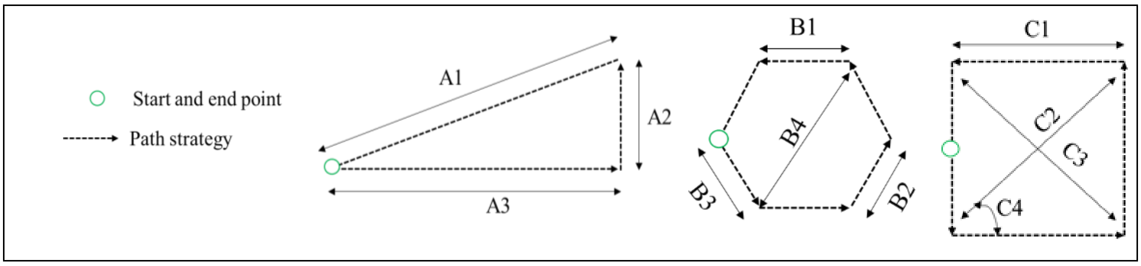

Figure 4.11 - Representation of the triangle, hexagon and square dimensions measured.

Table 4.13 - Measurements registered of the triangular shape.

Triangle nr.	Feeding Dimension [mm]			Measured Dimension [mm] μ ± σ		
	A1	**A2**	**A3**	**A1**	**A2**	**A3**
1	44.7	20	40	44.03 ± 0.21	19.83 ± 0.15	39.43 ± 0.15
2	89.44	40	80	88.49 ± 0.30	39.89 ± 0.10	79.76 ± 0.11
3	178.89	80	160	178.53 ± 0.28	79.66 ± 0.10	159.76 ± 0.06

Table 4.14 - Measurements registered of the hexagonal shape.

Hexagon nr.	Feeding Dimension [mm]				Measured Dimension [mm] μ ± σ			
	B1	**B2**	**B3**	**B4**	**B1**	**B2**	**B3**	**B4**
1	15	15	15	30	15.23 ± 0.06	14.83 ± 0.06	14.99 ± 0.10	30.03 ± 0.06
2	30	30	30	60	30.19 ± 0.10	29.69 ± 0.10	29.76 ± 0.21	59.76 ± 0.21
3	60	60	60	120	60.10 ± 0.10	59.76 ± 0.10	59.89 ± 0.10	119.73 ± 0.06

Table 4.15 - Measurements registered of the squared shape.

Square nr.	Feeding Dimension				Measured Dimension $\mu \pm \sigma$			
	C1 [mm]	C2 [mm]	C3 [mm]	C4 [◦]	C1 [mm]	C2 [mm]	C3 [mm]	C4 [◦]
1	20	28.28	28.28	45.00	19.8 ± 0.10	28.03 ± 0.11	27.87 ± 0.06	45.33 ± 2.50
2	40	56.57	56.57	45.00	39.66 ± 0.68	56.3 ± 0.10	56.23 ± 0.11	44.89 ± 1.10
3	80	113.14	113.14	45.00	79.63 ± 0.15	112.4 ± 0.26	112.93 ± 0.20	44.93 ± 0.57

Even though there is an error associated with the software used to measure dimensions, the backlash that appeared between movement reversals was noticed. However, the accuracy test has shown coincidence between end and start points for every geometry.

From the results of the triangle geometries, the measured dimensions were mostly lower than the feed ones. The biggest variation occurred in the dimension A1 of the first triangle that registered 0.67 mm with a standard deviation of 0.21 mm. The results for the hexagon geometry were also consistent, the biggest variation was on the dimension B2 at the second hexagon and it was 0.31 mm with a standard deviation of 0.1 mm. The square geometry originated the major values. They allowed to clarify that X and Y axis were correctly placed making 90º between each other. The results are satisfactory since the measured dimensions are within a range of 0.3 mm between the feeding dimensions.

Overall the positioning system shows high accuracy in the three axes. In the X and Y axis it was noticeable the effect of the backlash during unidirectional movement reversal, but for a WAAM application the system has an acceptable accuracy.

4.2 Speed tests results

Table 4.16 presents the results of the speed tests. Even though most of the results are below the theoretical value, it does not mean that the system runs lower than what it should be. The uncertainty associate with the error that the researcher commits when he clicks the time knob is much higher than the values of the smallest division of the scale where the reading is performed. From the results it is clear that independently of the travelling orientation and speed used, the values measured are within an acceptable range. A maximum deviation of 0.24 mm/s was attained in run nr.6.

Table 4.16 - Speed test results.

Run nr.	Travelling Speed [mm/s] Experimental $\mu \pm \sigma$	Travelling Speed [mm/s] Theoretical	a [mm]	Axis Tested
1	24.96± 0.10	25	1000	X
2	49.95 ± 0.11	50	1000	X
3	25.02 ± 0.07	25	1000	Y
4	49.76 ± 0.13	50	1000	Y
5	24.97 ± 0.09	25	1000	X and Y
6	49.87 ± 0.24	50	1000	X and Y
7	1.50 ± 0.01	1.5	100	Z
8	0.75 ± 0.085	0.75	100	Z

4.3 Vibration tests results

Results of the seven runs referenced previously in Table 3.6 were analyzed in the time domain and are given in Table 4.17**.**

Table 4.17 - Vibration tests results.

Run nr.	Maximum absolute displacement [mm]	X-axis [mm]	Y-axis [mm]	Z-axis [mm]	RMS [mm] X axis	RMS [mm] Y axis	RMS [mm] Z axis
1	0.85	[-0.87;0.80]	[-0.59;0.69]	[-0.50;0.50]	0.26	0.25	0.20
2	1.16	[-0.95;0.82]	[-0.71;0.71]	[-0.59;0.61]	0.28	0.25	0.24
3	1.14	[-0.85;0.77]	[-0.63;0.73]	[-0.62;0.76]	0.26	0.23	0.23
4	1.24	[-0.81;0.87]	[-0.82;0.84]	[-0.8;0.68]	0.29	0.31	0.29
5	0.07	[-0.05;0.06]	[-0.03;0.02]	[-0.03;0.02]	0.02	0.01	0.01
6	0.02	[-0.02;0.02]	[-0.02;0.02]	[-0.02;0.01]	0.01	0.01	0.005
7	0.44	[-0.19;0.26]	[-0.34;0.16]	[-0.11;0.23]	0.06	0.05	0.03

The sensor was correctly fixed during the entire process since the mean values of the acceleration series were nearly zero. The results of unidirectional movements and bidirectional movements on the X and Y axes are quite similar to each other. A maximum absolute displacement of 1.24 mm was reached at run nr.4. A maximum absolute displacement of 0.07 mm and 0.02 mm were measured in runs nr. 5 and 6, respectively, both represented unidirectional movements on the Z-axis. In run nr. 7, that illustrated a bi-directional movement, resulted in inferior values of RMS in every axis when compared to the unidirectional movements performed on the X and Y axes.

These displacements are a result of the large length between the tip of the welding torch and the screws that fasten it to the moving head. If needed the design of the welding torch should be rethought to decrease the overall dislocations. Nevertheless, the overall displacement values are low and do not affect substantially the welding fusion zone upon deposition.

The displacements in time domain resultant of the oscillations of the welding torch for run nr. 2 are presented in Figure 4.12, in which is visible the high displacements values upon start and end of the welding torch path.

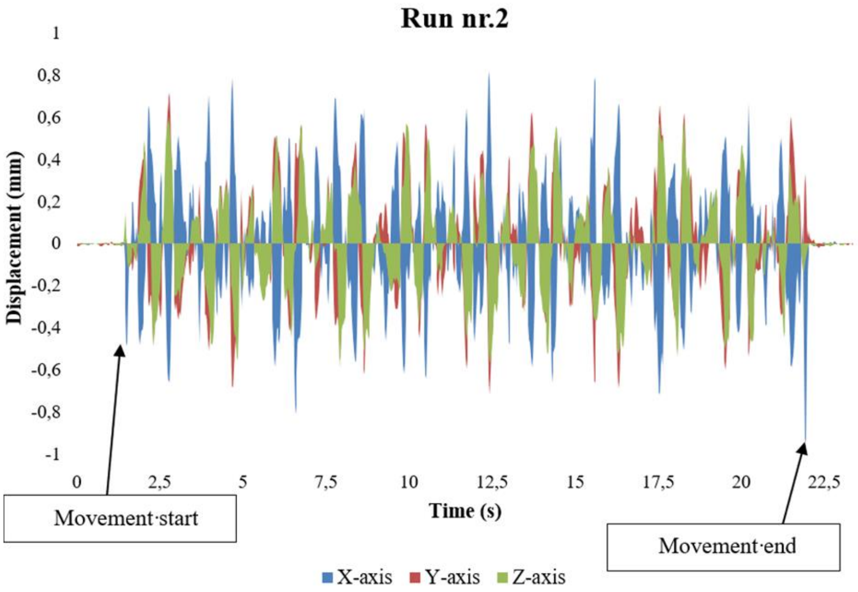

Figure 4.12 - Displacements recorded in the three axes in time domain of run nr.2.

4.4 Chapter resume

This chapter described the tests developed on the equipment, by quantifying accuracy, speed and vibration tests. The results obtained with the second methodology to validate equipment accuracy shown a maximum inaccuracy of 0.02 mm. Additionally, neither travelling speed, distance nor micro stepping ratio affect the positioning system performance. It was visible a backlash upon axis reversals from the X and Y linear guides, however its low value can be neglected since with repetitive turnaround, the moving head always returned to the starting point. Moreover, if a precision positioning system is required, the backlash value can be fed into the software. The equipment was also validated in terms of speed and a maximum deviation of 0.24 mm/s was recorded. Vibration test results were satisfactory since an RMS of 0.06 mm for a bi-directional movement was measured.

5

Parts manufactured by WAAM and its characterization

5.1 Experimental procedure

5.1.1 Material characterization

In this investigation, a commercial low carbon high strength steel AWS A5.28 ER110S-G wire electrode with a diameter of 1 mm was used. Originally developed for welding HY-80 and HY-100 steels, this wire is being used for welding, repairing ship builds, tools and dies industries and in power plants components. It exhibits a high tensile strength and fracture toughness. The wire chemical composition and mechanical proprieties are summarized in Table 5.1 and in Table 5.2, respectively [66].

Table 5.1 - Chemical composition of the ER110S-G wire electrode [wt.%] [66].

C	**Mn**	**Si**	**Ni**	**Cr**	**Mo**	**V**	**Cu**	**Fe**
0.08	1.70	0.44	1.35	0.23	0.30	0.08	0.25	Balance

Table 5.2 - Mechanical proprieties of the ER110S-G wire electrode [66].

Yield Strength [MPa]	Tensile Strength [MPa]	Elongation [%]	Impact ISO-V [J]	
			20 ºC	-40 ºC
750	790	22	>80	>47

Commercial pure Argon and a mixture of Argon-Helium-Carbon dioxide were used as shielding gases. The chemical composition of both is provided in Table 5.3.

Table 5.3 - Composition of the welding shielding gases.

Gas	Composition [% Vol. abs]			Impurities [ppm]		
Alphagaz 2	Ar			H_20	O_2	C_nH_m
	99.9999%			<0.1	<0.1	<0.1
Arcal 121	Ar	He	CO_2	H_2O (5bar)	O_2	N_2
	Balance	18% $\pm$ 1.8 %	1% $\pm$ 0.2 %	<40	<20	<80

The parts were built on mild steel substrates with dimensions of 190 x 100 x 10 mm previously cleaned and dried. Every substrate had the same dimensions, in order to avoid different heat dissipation conditions.

5.1.2 Buildup of samples

Samples were built using optimized processing parameters from previous work [41], varying also the number of layers in order to have parts with enough height to remove specimens for mechanical and microstructural characterization in two directions (Y and Z). The length of the walls was fixed at 170 mm with a contact tip to work distance of 6 mm. The cooling time between inter-layers was kept constant at 1 minute and parts were processed until 65 mm in height were achieved. Process parameters are given in Table 5.4.

Table 5.4 - Process parameters of the samples chosen to be reproduced [41].

Sample ref.	Gas	Flow rate [l/min]	WFS [m/min]	TS [mm/s]	Wave mode	Voltage [V]	Voltage regulation
P1	Alphagaz 1	16	2.5	9	Synergic Pulsed	n.a.	-6
P2	Arcal 121	8	3.0	3.9	Continuous	21	n.a.
P3	Alphagaz 1	16	3.0	9	Continuous	21	n.a.

A current probe *LEM LA 200-P* (Figure 5.1) was fixed to the ground cable to record the current. This probe acts according to the Hall effect. Electrons moving through the ground cable towards the probe cause a deflection of the charge carriers and, as a consequence, a difference in the voltage is induced by the changes of the magnetic field of the probe.

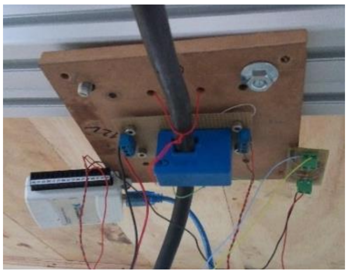

Figure 5.1 - LEM LA 200-P current probe.

Since the data acquisition system was just capable to measure $\pm$ 10 V a set of resistances connected in series with a reduction ratio of 31 allowed to measure the Voltage during depositions well above 10 V.

5.1.3 Infrared thermography

A thermography camera *Fluke TI400* monitored the temperature of the beads during depositions. The temperature range was set up to a maximum of 1200°C, with a measurement accuracy of ± 2°C, with an infrared spectral band up to 14 μm and a refresh rate of 9 Hz. Videos of the complete depositions were recorded and *SmartView* software allowed to process data acquired at different points of each deposited layer. These data were later analyzed to calculate cooling rates experienced by the material during sample build up.

The infrared thermography camera setup is illustrated in Figure 5.2.

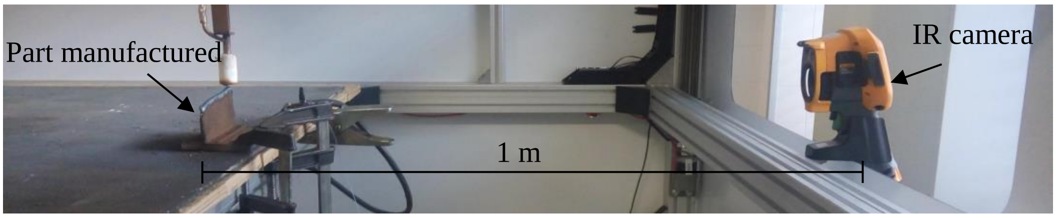

Figure 5.2 - Infrared thermography camera setup on WAAM equipment.

The *Stefan-Boltzmann law* (equation 5.1) describes the principle of the infrared temperature measurements:

$$E_T = \varepsilon \cdot \sigma \cdot T^4 \tag{5.1}$$

Where E_T, is the energy radiated per unit area per unit time [$J\, m^{-2} s^{-1}$], σ, is the Stefan-Boltzmann constant [$5.67 \times 10^{-8}\, J\, s^{-1}\, m^{-2}\, K^{-4}$], T is the body's thermodynamic temperature, ε is the emissivity of the surface which varies from 0 to 1. It is well known that the emissivity of an object depends on the temperature, especially at high temperature, as those observed in fusion welding. An emissivity of 0.84 was used [67].

5.1.4 Deposition strategy

The deposition strategy used consisted of a single pass multi-layer deposition strategy. The torch moved in the Y-axis while the ER110G-S steel wire was being deposited. After one layer the torch ascend a height equal to a bead height in the Z-axis and returned always to the same starting point.

As the number of layers increases excessive heat sink at the beginning of the deposition is observed that decreases the weld penetration as illustrated in Figure 5.3. In contrast, at the end of the layer low heat dissipation due to high temperatures results in layer height drop. To overcome this issue, the current and travel speed should be higher in the beginning and reduced gradually at the end of the deposition [68].

The current system did not allow to adjust the current. However, it was possible to adjust the speed in the beginning and in the end of each layer. Therefore, in the first 10 mm the travel speed was lowered by 30% and increased by 30% in the last 10 mm of every layer.

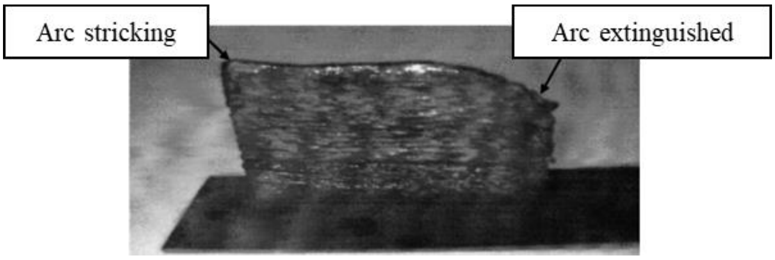

Figure 5.3 - Wall appearance without travelling speed control [68].

Figure 5.4 illustrates the deposition strategy adapted for the depositions of this work. The green lines represent the deposition path, and the red lines the torch movement with the torch off. The torch deposited material along the longitudinal direction (Y) and walls were build up in the normal direction (Z).

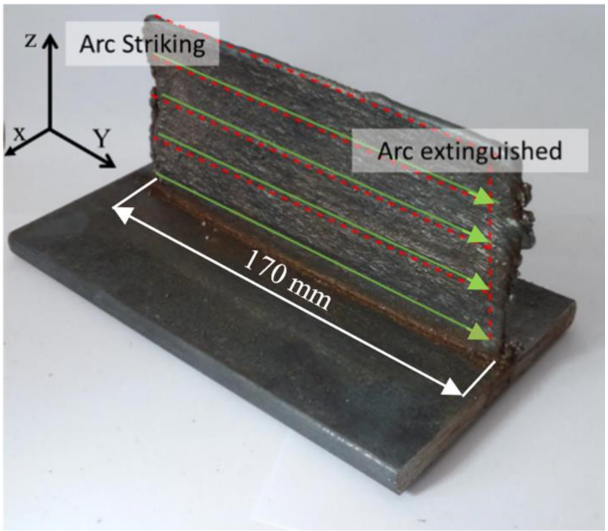

Figure 5.4 - Deposition strategy of this work single walls.

5.1.5 Heat input and deposition rate calculation

In arc welding process, the heat input (HI) provides the information of how much energy has been transferred from the arc to the workpiece or previous beads. It is measured in units of energy per unit of length [J/mm], providing a relevant parameter to compare different depositions. Being, U, the RMS of the voltage [V], I, the RMS of the current [A], η, the efficiency of the welding process (80% for arc welding) and TS, the travel speed of the torch [mm/s]. The heat input can be calculated accordingly to equation 5.2.

$$\mathrm{HI} = \frac{\mathrm{V} \times \mathrm{I}}{\mathrm{TS}} \cdot \eta \qquad [\mathrm{J/mm}] \tag{5.2}$$

The deposition rate (DR) calculation was made by dividing the weight of one layer by the time of its duration. As summarized in equation 5.3, where L is the length of wire extruded in each layer [m], D is the wire diameter [m], ρ the density of the consumable wire [Kg/m^3] and DT the time of its deposition [h]. DR expresses how much consumable material is being deposited on open arc for one hour.

$$\mathrm{DR} = \frac{\mathrm{L} \times \pi \mathrm{D}^2 \times \rho}{4 \times \mathrm{DT}} \qquad [\mathrm{Kg/h}] \tag{5.3}$$

5.2 Characterization techniques

5.2.1 Visual inspection

Visual inspection was the first non-destructive test performed to identify defects on the samples before any further tests.

It allowed to detect inconsistent layer cross-section dimensions (Figure 5.5a), defects between layers such as undercuts or excessive melting, and variations in dimensions of the parts, especially at the final stage that can lead to porosity as seen in Figure 5.5b.

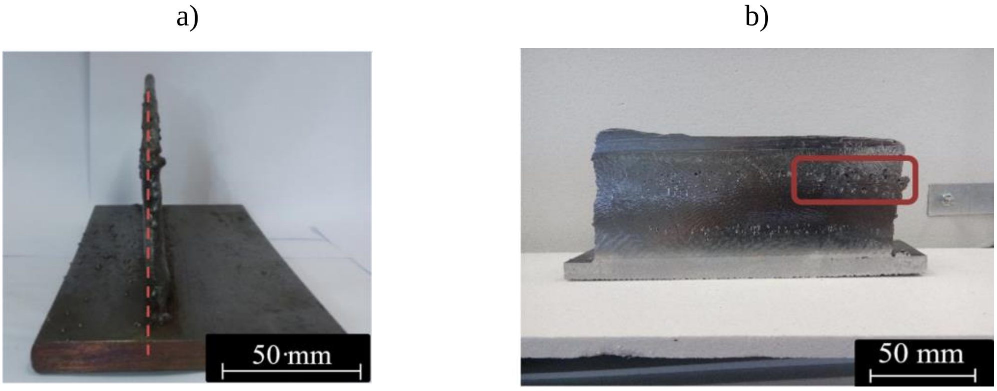

Figure 5.5 - Typical defects that may occur during WAAM depositions: a) Inconsistence wall thickness, b) Variation of final part height and porosity.

5.2.2 Surface waviness measurement

Surface Waviness (SW) is one of the most important parameters to evaluate the quality of depositions. As defined in the literature [17] it is the maximum peak-to-valley distances measured from a profile of a given area in the wall (see Figure 5.6). Surface waviness was measured resorting the image treatment software *Adobe Photoshop CS6*.

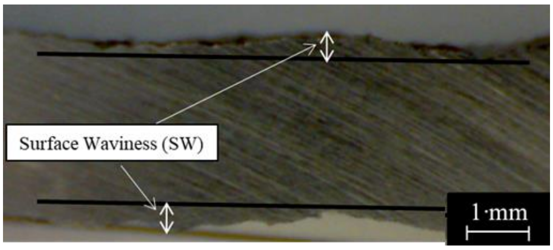

Figure 5.6 - Surface waviness measurement representation.

For each sample fabricated five measurements of each width, height and peek were performed in order to present the respective mean and standard deviation values.

5.2.3 Sample preparation

Specimens were removed by mechanical cutting for subsequent microstructural (optical microscopy and hardness measurements) and mechanical testing (tensile and impact tests). Cutting was performed in a *MELDAS VMC 50* machining center.

5.2.4 Metallographic analysis

To evaluate possible gradients of macro and microstructure along samples height, as well as to identify possible defects, grain morphology and size a macro and microscopic analysis was performed with a *Leica DMI 5000 M* inverted optical microscope available at CENIMAT/i3N, Materials Science Department of FCT-NOVA.

To investigate the relationship between microstructural evolution and mechanical properties within the buildup wall, metallographic specimens were taken from the start, middle and end regions of the deposited walls (Figure 5.7a). Each cross section was observed in five distinct zones along the height, marked with an X in Figure 5.7b. Specimens were cut, polished and etched with Nital (3%) for observations.

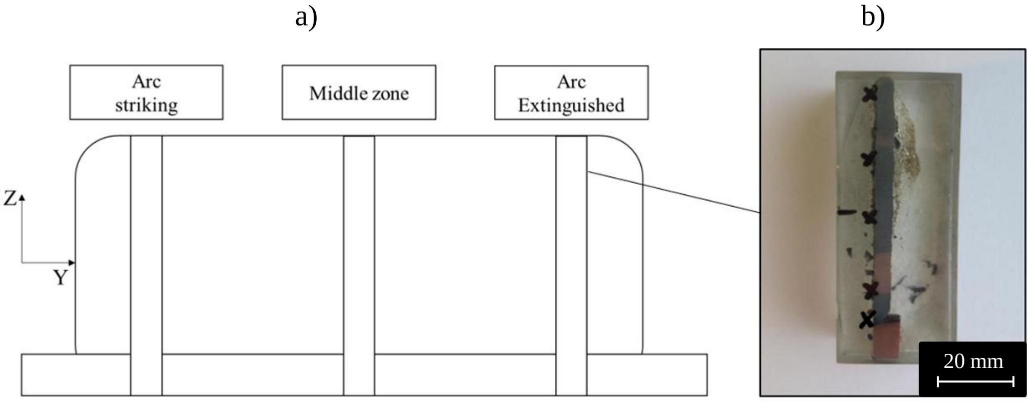

Figure 5.7 - a) Illustration of the removed sections zones b) Cross sections observed macro and microscopically.

5.2.5 Microhardness measurements

The specimens selected for microscopic analysis were used for microhardness measurements allowing to identify the distinct types of microstructure along the specimen.

Microhardness indentations were made with a *Mitutoyo HM-112 Micro-Vickers Hardness Testing Machine* available at DEMI-FCT NOVA. The indentations were performed under a load of 5N for 10 s in four distinct zones along the height and the width of the specimens with a distance between them of 200 μm.

These measurements enable to analyze the evaluation of hardness along the height and width due to the imposed thermal cycles and heat accumulation.

5.2.6 Uniaxial tensile tests

Tensile tests were made with a hydraulic press model *MTS* with a capacity of 100 kN available at the Laboratory of Structural Mechanics of DEMI-FCT. The elongation was measured by an extensometer placed on tensile specimens, the maximum load was given by the machine software and tests were performed with a load speed of 0.017 mm/s.

Longitudinal and transversal flat samples with dimensions given in Figure 5.8 were removed from each wall manufactured from the zones depicted in Figure 5.9.

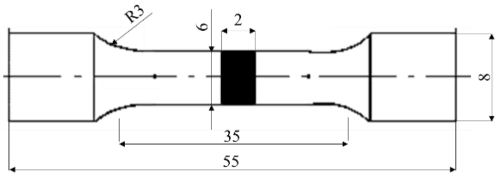

Figure 5.8 - Uniaxial tensile test specimen dimensions.

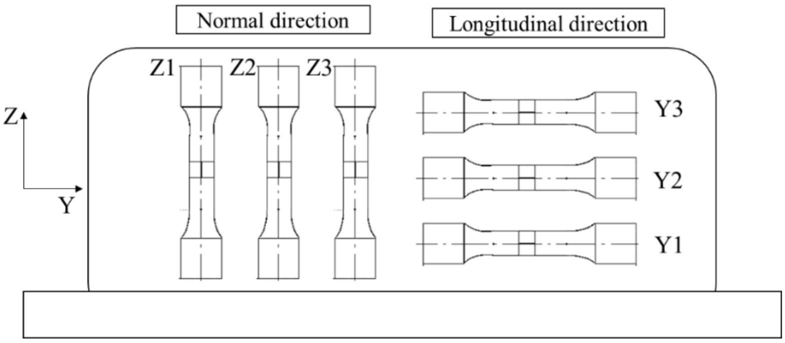
Normal direction
Longitudinal direction
Z1
Z2
Z3
Y3
Y2
Y1
Z
Y

Figure 5.9 - Uniaxial tensile tests specimens location.

5.2.7 Charpy impact energy test

Reduced specimens for Charpy impact tests were removed and tested according to ISO 148- 1:2016. Test pieces were 55 x 10 x 2.5 mm with a 2 mm deep V-notch and were tested at 20 ºC. Three samples were removed from the zones shown in Figure 5.10 allowing for statistical analysis. Tests were performed in LabMat of *Instituto de Soldadura e Qualidade* (ISQ).

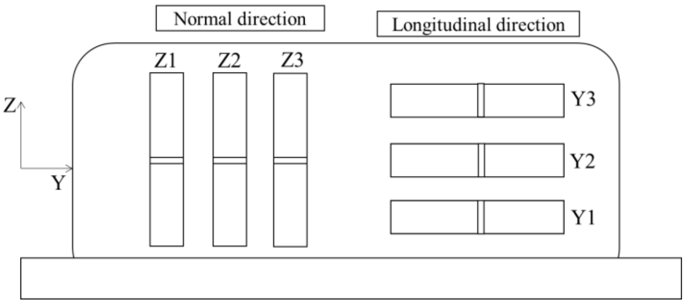
Normal direction
Longitudinal direction
Z1
Z2
Z3
Y3
Y2
Y1
Z
Y

Figure 5.10 - Charpy impact energy test specimens location.

5.2.8 Scanning electron microscopy

Additional observations were conducted in Scanning Electron Microscope (SEM) *ZEISS DSM 962 ESM,* available at CENIMAT in Material Science Department.

These observations had several objectives: investigate the fracture mode of the material produced, assess if elemental composition had changed due to AM procedure, investigate the existence of internal defects and precipitates. The same sample used on microhardness test was submit to this analysis in the same 4 zones of the hardness test and additionally in the HAZ between the first layers and the substrate, as depicted in Figure 5.11.

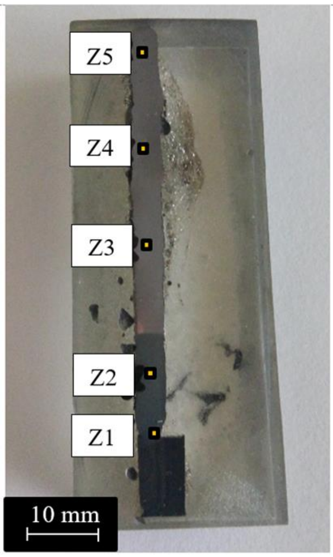

Figure 5.11 - EDS analyzed points.

Fracture surface analysis of a uniaxial tensile specimen was performed with secondary emitted radiation. Compositional heterogeneities were investigated with BSE (back-scattered electrons) scanning modes with an energy dispersive X-ray spectrometry (EDS) from Oxford Instruments, INCA X-ACT) associated to SEM. In both observations an energy of 20 keV was used.

5.3 Chapter resume

This chapter describes the experimental procedure adopted to manufacture parts by WAAM with the equipment described in Chapter 3 and the procedure adopted with the tools available at FCT-UNL that are adequate from a mechanical engineering perspective to perform parts characterization.

6

Results and discussion of manufactured parts and its characterization

6.1 Macroscopic characterization

The repeatability of the developed equipment and welding torch was guaranteed by repeating the production of each sample twice, using optimized processing parameters from previous work [40]. Figure 6.1 presents the overall aspect of manufactured samples, reference P1, P2 and P3, as well as their transversal cross sections.

a)

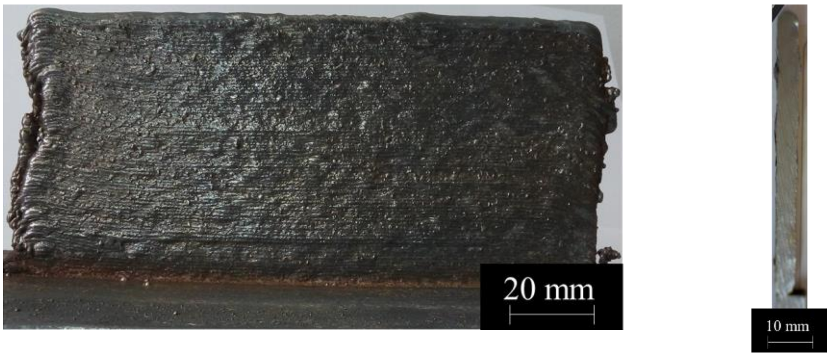

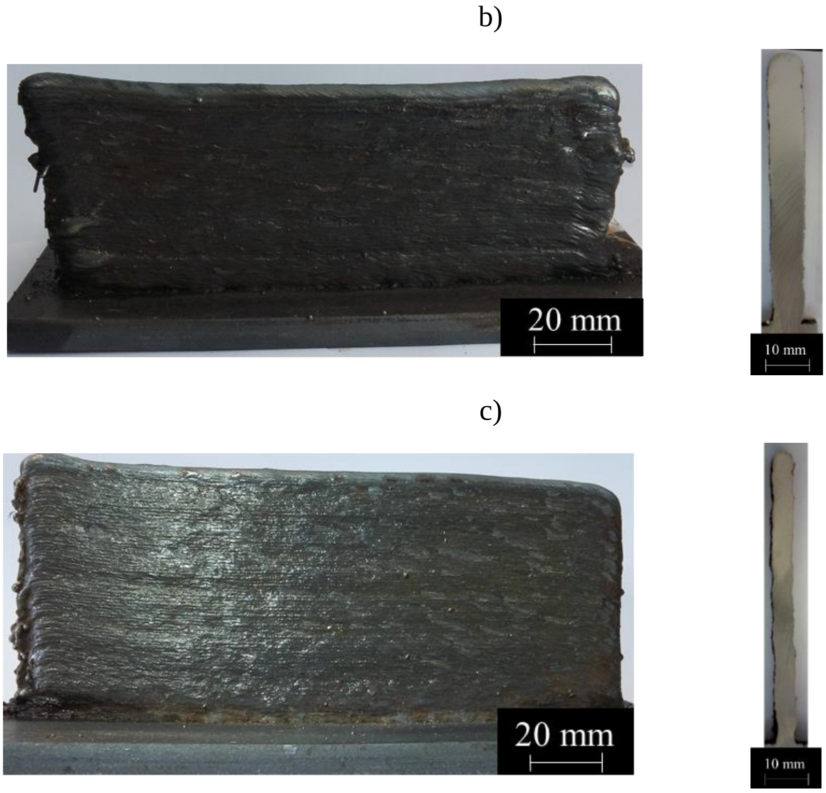

Figure 6.1 - Produced parts aspect and corresponding transversal sections of samples: a) P1, b) P2 and c) P3.

The difficulties associated to control the contact tip to work distance in the beginning of each layer, originated an inconsistent arc starting position and this effect is visible on the left side of each wall. It is also visible a narrow bead width in the first layers of each cross section, due to rapid cooling to the cold substrate and the low amount of heat accumulated due to previous weld beads. Results of width, height per layer, waviness and heat input of each sample are given in Table 6.1.

Table 6.1 - Results of width, height, waviness, deposition rate and heat input for each deposition.

Sample Reference	**Deposition Rate [Kg/h]**	**Heat Input [J/mm]**	**Waviness [µm] µ ± σ**	**Width [mm] µ ± σ**	**Height of each layer [mm] µ ± σ**
P1	0.92	101.96	401.56 ± 63.32	4.23 ± 0.12	0.92 ± 0.02
P2	1.11	462.68	355.46 ± 15.55	8.82 ± 0.55	1.34 ± 0.05
P3	1.11	166.98	546.16 ± 65.79	5.63 ± 0.26	0.93 ± 0.03

Part P2 was built with the highest wire feed speed and lowest travelling speed, resulting in a wider portion of material being deposited per layer in the sample with highest heat input. It is also the sample with lowest surface waviness due to the higher interpass temperature (temperature of previously deposited layer upon deposition of a subsequent layer) experienced. Its roughness is explained by its higher heat input that increases the interpass temperature improving wettability of subsequent layer and the existence of CO_2 in the shielding gas that improves bead penetration. In order to obtain less surface waviness in the other samples, the interpass time should be decreased so that the temperature of previous deposited layer would raise. Such increase would hinder the formation of an oxide film between layers improving the wettability of the molten metal [42].

As previously explained the travel speed varied during each layer deposition in order to compensate the heat transfer differences during parts building. This compensation allowed to have walls with an almost constant height (Table 6.2**)**.

Table 6.2 - Comparison between height at arc start and end with the travel speed compensation.

Sample	Height at arc striking [mm]	Height at arc extinguished [mm]
P1	61.9	54.7
P2	78.2	67.3
P3	65.4	61.7

P1 and P3 samples, both with lower heat input than P2, shown height differences of 7.2 and 3.7 mm, respectively. However, sample P2 characterized by a high heat input, the height control was more difficult, and a variation of 10.9 mm was recorded.

Apart from the strategy described [68] others can be adopted to mitigate the height variation at arc striking to arc extinguished position with the existent setup. For sample P2 characterized by a high heat input the interpass time should increase to mitigate these differences of part height. However, as seen before increasing interpass time result in a rougher surface. Furthermore, instead of compensations of the travelling speed by 30% other percentages should be studied or increase the length of this compensation from 10 mm to a higher value.

6.2 Thermal analysis

The heat is dissipated by conduction, convection and radiation to the surrounding atmosphere. However, cooling through conduction becomes difficult as the number of layers increase, since the large area of substrate facilitates heat dissipation in the initial layers. The heat transfer to the underlying layers is of major concern since it will affect the cooling rates and the thermal cycles. Both aspects can be controlled so that the desired microstructure and mechanical proprieties are achievable. Moreover, subsequent passes of the welding torch coarse the grains and reduce residual stresses by post heat treatments.

Thus, different cooling rates are experienced during a deposition and lead to the formation of different grain size, phase morphology and precipitates. In order to evaluate the evolution of the cooling rate along a wall being deposited, monitoring of temperature was performed at different points along the height at the center of the part (Figure 6.2).

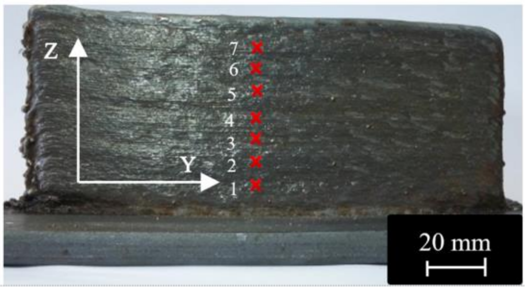

Figure 6.2 - Schematic illustration of the temperature measurement points.

Table 6.3 and Table 6.4 depicts the cooling rates due to subsequent passes above the tracking points, for sample P2 and P3, respectively. These cooling rates were measured by calculating the average temperature gradient from 800 to 500 ºC, since it was experimentally observed that the cooling rate is constant within this temperature range [69]. Some of the subsequent passes did not introduce enough energy to heat the previous layers above 500ºC, in those cases the cooling rate was not registered. Due to the similarities of heat input between P1 and P3 depositions, the thermal behavior was only registered for the second one.

As expected, the sample fabricated with higher heat input deposition (P2) caused lower cooling rates than sample P3. Moreover, for both depositions the large area of the substrate facilitates heat dissipation resulting in higher cooling rates at the first layers that decrease with the increase of the number of layers. From these values, it can be seen that there is a trend for stabilization of the cooling rate at a certain point. A stable state was reached around the third tracking point for part P2, in contrast with sample P3 a constant heat dissipation state was only reached around the sixth tracking point.

To illustrate the information contained in both tables, Figure 6.3 depicts the cooling rates computed for the fourth tracking point of specimen P3, in which is visible the effect of sixteen subsequent passes and can be concluded a decrease of the temperature peaks and cooling rates with the increase of the distance to the weld pool.

Table 6.3 - Cooling rate [Cº/s] of sample P2.

		Tracking point number:						
		1	**2**	**3**	**4**	**5**	**6**	**7**
Number of layer deposited above the tracking point:	**1**	47.36	9.62	6.37	6.29	5.85	5.47	5.23
	2	10.97	7.27	5.69	5.50	4.96	5.5	4.22
	3	9.18	6.15	5.45	5.13	4.78	5.28	5.15
	4	7.69	5.47	5.14	5.21	4.51	4.92	5.90
	5	6.63	5.73	4.77	4.86	4.01	4.72	3.86
	6	5.82	5.70	4.69	4.81	4.33	4.50	n.a.
	7	5.38	4.93	4.50	5.05	3.97	3.81	n.a.
	8	4.71	4.39	4.26	4.74	4.48	3.62	n.a.
	9	3.41	3.80	4.63	4.63	4.53	3.59	n.a.
	10	3.04	3.35	4.13	4.11	4.53	3.53	n.a.
	11	2.70	2.86	3.55	3.72	4.12	3.26	n.a.
	12	2.30	2.43	3.91	3.59	4.27	n.a.	n.a.
	13	2.01	2.08	3.43	3.40	3.37	n.a.	n.a.
	14	1.97	1.85	3.17	3.27	3.05	n.a.	n.a.
	15	n.a.	1.74	3.03	2.97	2.01	n.a.	n.a.
	16	n.a.	1.63	2.93	2.64	1.60	n.a.	n.a.
	17	n.a.	1.59	2.65	2.31	1.80	n.a.	n.a.
	18	n.a.	1.29	2.48	2.20	1.68	n.a.	n.a.
	19	n.a.	1.32	2.26	1.95	0.977	n.a.	n.a.
	20	n.a.	1.14	2.35	1.82	n.a.	n.a.	n.a.
	21	n.a.	1.23	1.98	1.73	n.a.	n.a.	n.a.
	22	n.a.	n.a.	1.65	1.53	n.a.	n.a.	n.a.
	23	n.a.	n.a.	1.56	1.27	n.a.	n.a.	n.a.
	24	n.a.	n.a.	1.50	1.11	n.a.	n.a.	n.a.
	25	n.a.	n.a.	1.33	1.02	n.a.	n.a.	n.a.
	26	n.a.	n.a.	n.a.	1.12	n.a.	n.a.	n.a.
	27	n.a.	n.a.	n.a.	0.95	n.a.	n.a.	n.a.

Table 6.4 - Cooling rate [Cº/s] of sample P3.

	Tracking point number:						
Number of layer deposited above the tracking point:	**1**	**2**	**3**	**4**	**5**	**6**	**7**
1	58.60	19.42	18.18	12.85	12.11	11.06	10.45
2	48.06	15.64	13.20	11.86	11.17	10.07	9.73
3	43.39	14.91	12.56	11.08	10.77	9.44	8.82
4	9.22	10.62	12.44	10.93	9.40	9.12	8.70
5	7.77	11.08	11.22	10.21	8.91	8.82	8.57
6	5.22	9.27	10.70	9.68	8.85	7.91	7.72
7	n.a.	7.85	9.32	8.22	7.86	6.48	6.68
8	n.a.	6.72	7.59	6.98	6.41	5.91	5.63
9	n.a.	5.93	6.52	5.93	5.58	5.00	5.00
10	n.a.	4.96	6.08	5.24	4.90	4.53	4.44
11	n.a.	3.92	4.92	4.56	4.39	4.03	3.95
12	n.a.	n.a.	4.30	4.13	3.88	3.66	3.56
13	n.a.	n.a.	3.95	3.76	3.55	3.37	3.43
14	n.a.	n.a.	3.53	3.35	3.27	3.03	2.45
15	n.a.	n.a.	n.a.	2.83	2.97	2.15	2.15
16	n.a.	n.a.	n.a.	2.57	2.09	2.03	1.3

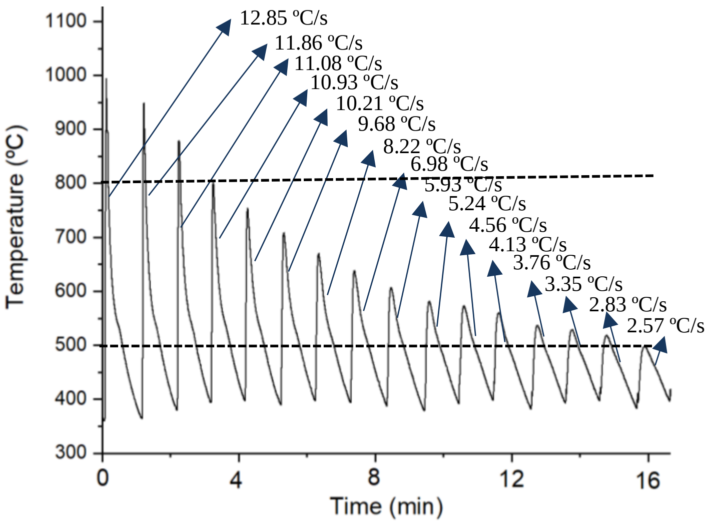

Figure 6.3 - Sequence of thermal cycles on the 4th tracking point of the P3 deposition.

The thermal history was important for determining the amount of time the material in a certain temperature range underwent solid state transformations. For that purpose, the residence time between 800-500 ºC was measured, in which solid state transformations occur in steels [11]. Results can be seen in Table 6.5.

Table 6.5 - Residence time [s] between 800ºC and 500ºC.

Tracking Point	**$t_{800-500\,^{\circ}C}$ [s] for sample:**	
	P2	**P3**
1	1089	48
2	1653	235
3	1903	362
4	1730 (until cooling of last layer)	459
5	1308 (until cooling of last layer)	516
6	757 (until cooling of last layer)	520
7	410 (until cooling of last layer)	549

The results of measuring the residence time between 800ºC and 500ºC were very interesting and it is visible that high heat input process resulted in longer residence times above a certain temperature. For the sample P2, from the fourth tracking point until the end of the process the temperature was always above 500ºC. Consequently, the last tracking points underwent less thermal cycles resulting in less time between that temperature period for upper tracking points.

For higher heat input the HAZ will be greater causing remelting of a wide portion of material. Figure 6.4 shows the area of the HAZ on the last layers of both depositions using the same temperature scale. As expected the deposition with higher heat input produced a larger HAZ.

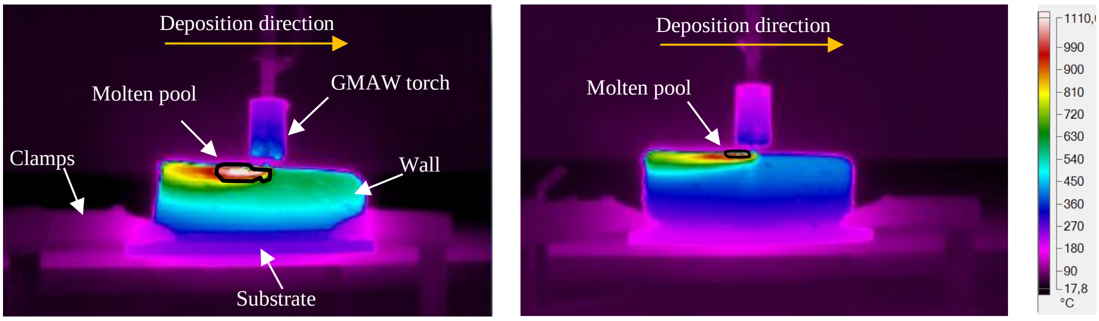

a)

b)

Figure 6.4 - Comparison between the HAZ area of samples: a) P2, b) P3.

The interpass temperature is considered as one of the most important aspects regarding surface waviness and temperature distribution of the parts during fabrication, so it should be consciously selected to avoid undesirable contamination of the oxides coming from previously layers surface [42,67].

The growth of the interpass temperature for sample P2 and P3 is presented in Table 6.6.

Table 6.6 - Growth of interpass temperature [°C] of P2 and P3 depositions.

Upon deposition of layer nr.	P2	P3
5	226	144
10	335	220
15	497	247
20	556	303
25	564	318
30	562	343
35	565	365
40	557	380
45	562	398
50	578	397
55	n.a.	411
60	n.a.	424
65	n.a.	423
70	n.a.	418
75	n.a.	422
80	n.a.	415

Concerning interpass temperature analysis, from the measurements obtained, the temperature continues to increase and reaches an equilibrium value. For sample P3 a steady state was reached around the 55^{th} layer in contrast of the P2 sample that reached a stable interpass temperature near the 20^{th} layer. With the increase of P2's numbers of layers deposited, the interpass temperature increases faster than in sample P3, due to the high heat input transferred to previous layers. This type of control based on interpass temperature is not appropriate, since some of the suitable dwell times may be too long reducing deposition productivity or too small that can only be achieved with the use of multiple welding torches, for example.

6.3 Microscopic characterization

During microscopical observations samples produced were fully dense without the presence of welding defects, such as cracks, porosity or lack of fusion. Typically, these HSLA steels experience cold cracking, a very common discontinuity that occurs when simultaneously exist:

- Brittle microstructure as martensite, due to rapid cooling;
- Hydrogen trapped in the heat-affected zone;

- Residual stresses.

The solubility of hydrogen in α-ferrite is lower than in the γ-austenite but its diffusion is higher in the ferrite than in the austenite. Additionally, the low carbon content promotes the transformation of γ→α for temperatures higher than the ones typical of the HAZ. Thus, the increase of hydrogen ions in ferrite becomes more likely to diffuse to austenite in HAZ, where its high solubility at austenite (more interstitials in a compact crystal lattice) causes its retainment in this phase before the solid state transformation to martensite occurs. The formation of molecular hydrogen from atomic accumulation causes high pressures that can lead to cracking upon cooling since the martensitic matrix has very poor ductility.

Typically, the influence of the chemical composition on the steel hardening and cold cracking is characterized by means of the carbon equivalent (C_{eq}). Each element affects the hardenability differently, and this empirical equation translates this by relating the combined effects of different alloying elements by means of equation (6.1) [70]. Steels with a high carbon equivalent are more likely to experience cold cracking, since they are more prone to form martensitic microstructures.

$$C_{eq}(\%) = C + \frac{Si}{25} + \frac{Mn + Cu}{16} + \frac{Cr + Ni}{20} + \frac{Mo}{40} + \frac{V}{15} \tag{6.1}$$

Another important aspect to take into consideration when predicting hardenability in welding is the maximum hardness (HV_{max}) below a weld bead. This value is highly dependent on the Carbon quantity which specifies martensitic hardness. Furthermore, it is also influenced by other elements such as Manganese, Silicon, Nickel and Chromium. The HV_{max} can be empirically calculated by means of equation 6.2 [70].

$$HV_{max} = 90 + 109\,C + 47\,Si + 75\,Mn + 30\,Ni + 31\,Cr \tag{6.2}$$

In welding literature there are many recognized procedures to mitigate cold cracking and most of them are intuitively used in WAAM, including pre and post heating. This effect is settled by the repetitive re-heating of previously deposited layers, that allows to reduce the cooling rate, and subsequently formation of martensite. Another factor that avoid this type of failure is the non-existence of welding joints restraints. Moreover, the low content of carbon difficult the formation of martensite. The combination of all these factors resulted in the suppression of this type of failure for this high strength low alloy electrode with a C_{eq} of 0.31 and a HV_{max} of 295 HV.

Figure 6.5c depicts the gradient of microstructure of the first layers deposited, in which can be distinguished the substrate, HAZ and the first layers. It is well known that the grain morphology of AM parts is columnar aligned along the buildup direction. However, equiaxed grain structures are desired since it can help reduce solidification cracking, improving mechanical properties. It is clear from Figure 6.5a, b the existence of columnar grains in the longitudinal direction along sample P2 height, these columnar grains form by epitaxial growth from the substrate. It is also visible columnar grains and continuity between adjacent layers being possible to identify two different regions: the HAZ and the re-melted zone (RZ).

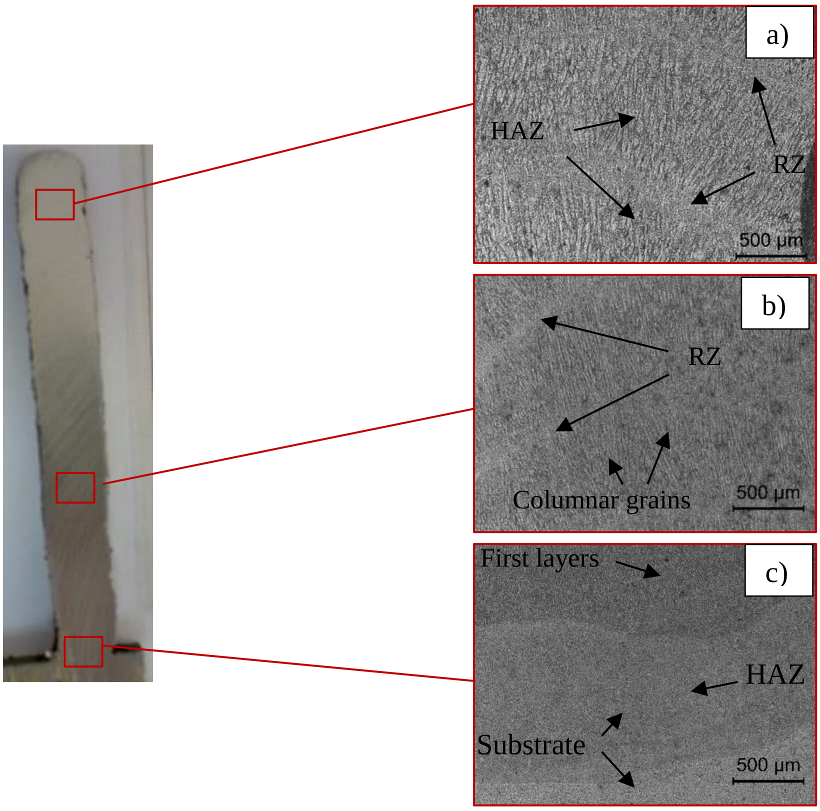

Figure 6.5 - Macrostructure along the height of sample P2 (HAZ: heat affected zone, RZ: re-melted zone).

A comparison between the microstructure of high and low heat input deposition, samples P2 and P3, respectively is illustrated in Figure 6.6 and Figure 6.7.

The microstructures are mostly constituted of ferrite and perlite. Ferrite has acicular and granular morphologies, while perlite shows different degrees of coarseness and these are intrinsically related to the cooling rates observed. It must be noticed however, that martensite in not present as expected after the previous explanation.

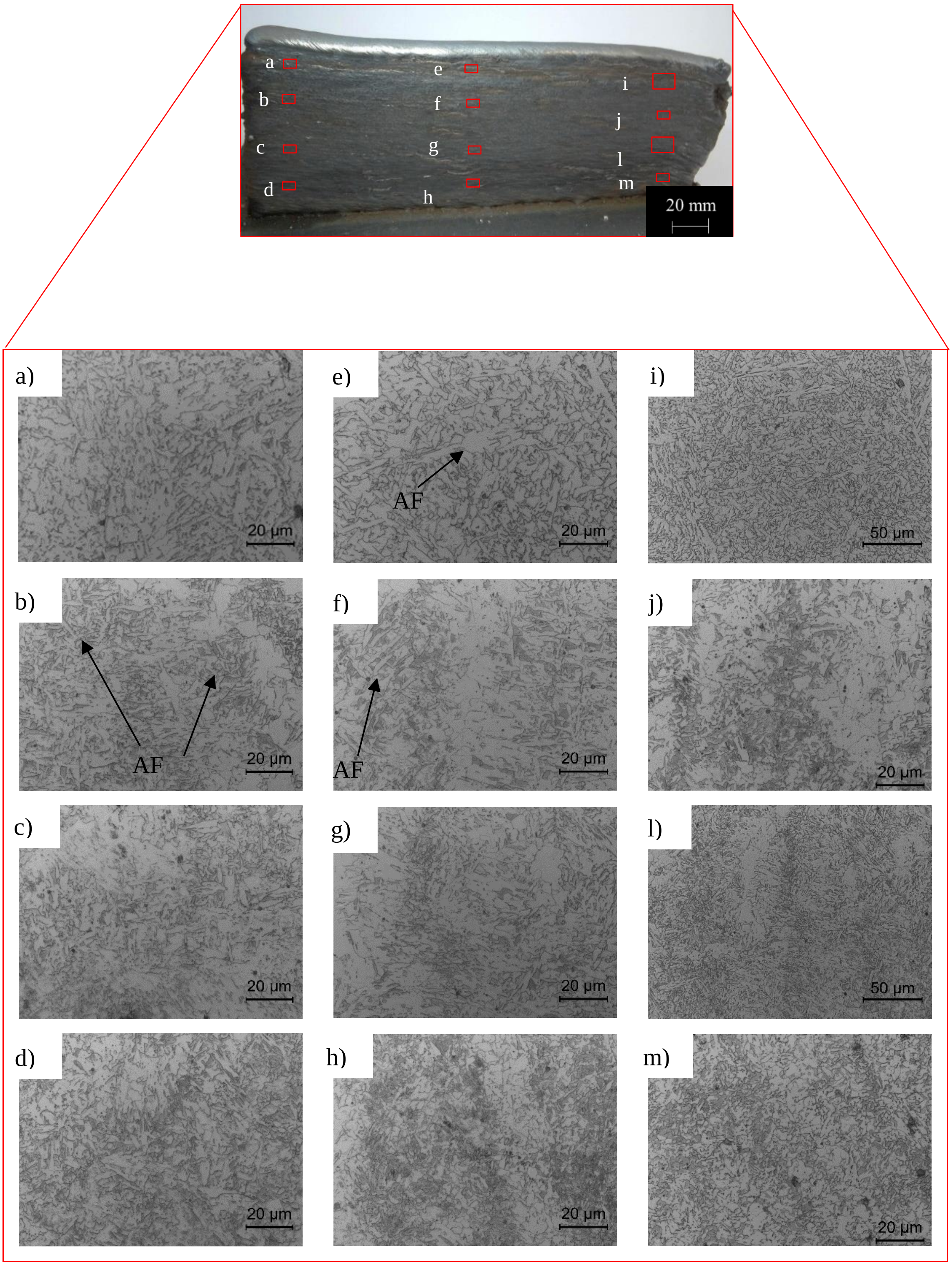
a
b
c
d
e
f
g
h
i
j
l
m
20 mm
a)
20 µm
e)
AF
20 µm
i)
50 µm
b)
AF
20 µm
f)
AF
20 µm
j)
20 µm
c)
20 µm
g)
20 µm
l)
50 µm
d)
20 µm
h)
20 µm
m)
20 µm

Figure 6.6 - Cross section micrographs of sample P2 in 12 distinct zones (AF: acicular ferrite).

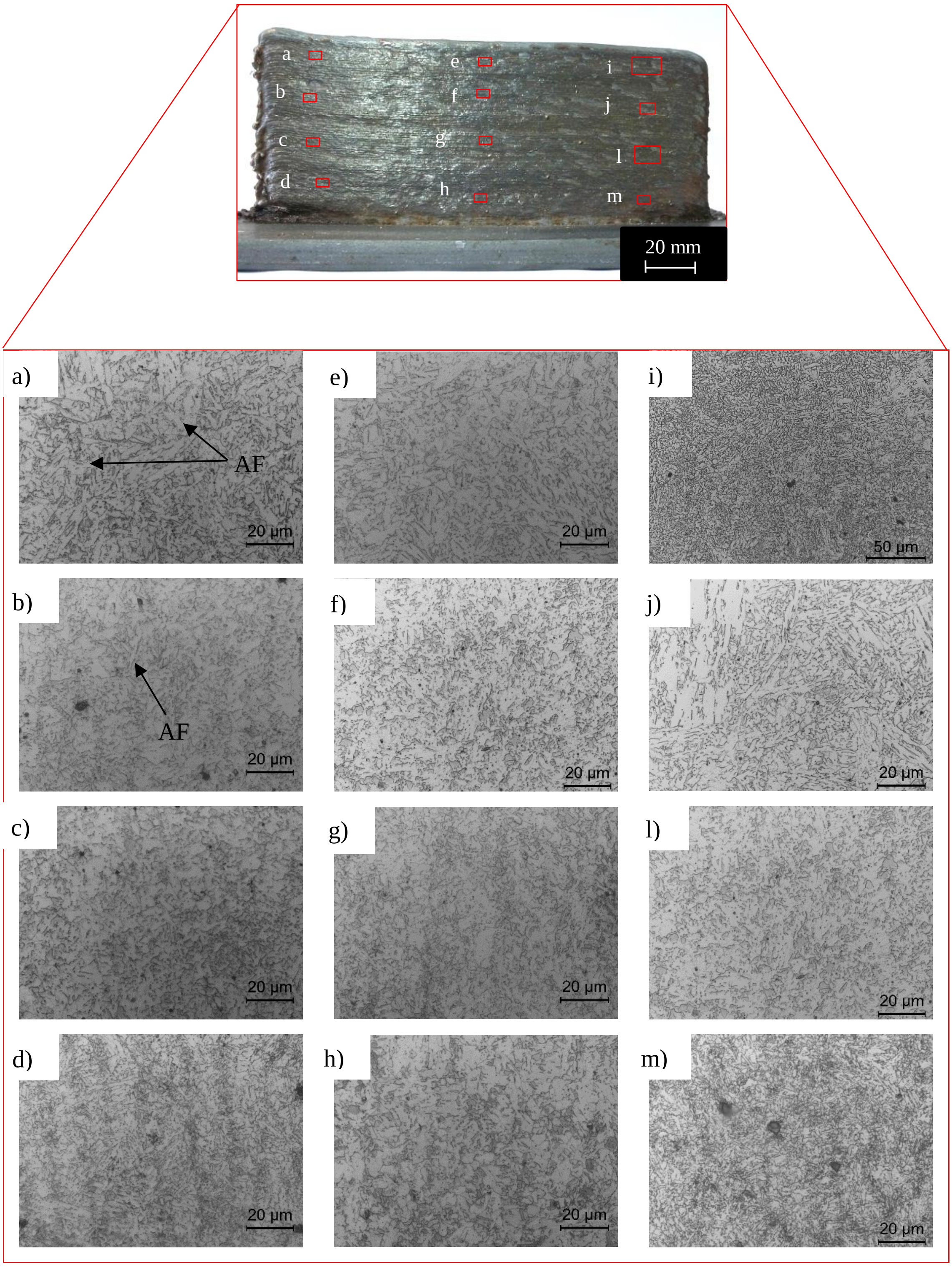
a
e
i
b
f
j
c
g
l
d
h
m
20 mm
a)
AF
20 µm
e)
20 µm
i)
50 µm
b)
AF
20 µm
f)
20 µm
j)
20 µm
c)
20 µm
g)
20 µm
l)
20 µm
d)
20 µm
h)
20 µm
m)
20 µm

Figure 6.7 - Cross section micrographs of sample P3 in 12 distinct zones (AF: acicular ferrite).

As a result of additional thermal cycles, grain became larger near top surface. Moreover, it is noticeable the differences regarding grain size between sample P2 (about 5 µm) and sample P3 (about 3.5 µm) near the top surface zone. Grain is larger in the P2 depositions due to a higher heat input experienced. It is also visible a microstructural homogeneity between the three studied zones (arc striking, middle zone and arc extinguished) at the same height, in both depositions.

Analyzing the Continuous Cooling Transformation (CCT) diagram (Figure 6.8) for an HSLA steel with a carbon content of 0.06 wt.% and a C_{eq} of 0.29 [71], the different microstructures can be analyzed. However, this CCT does not consider the successive thermal cycles of depositions.

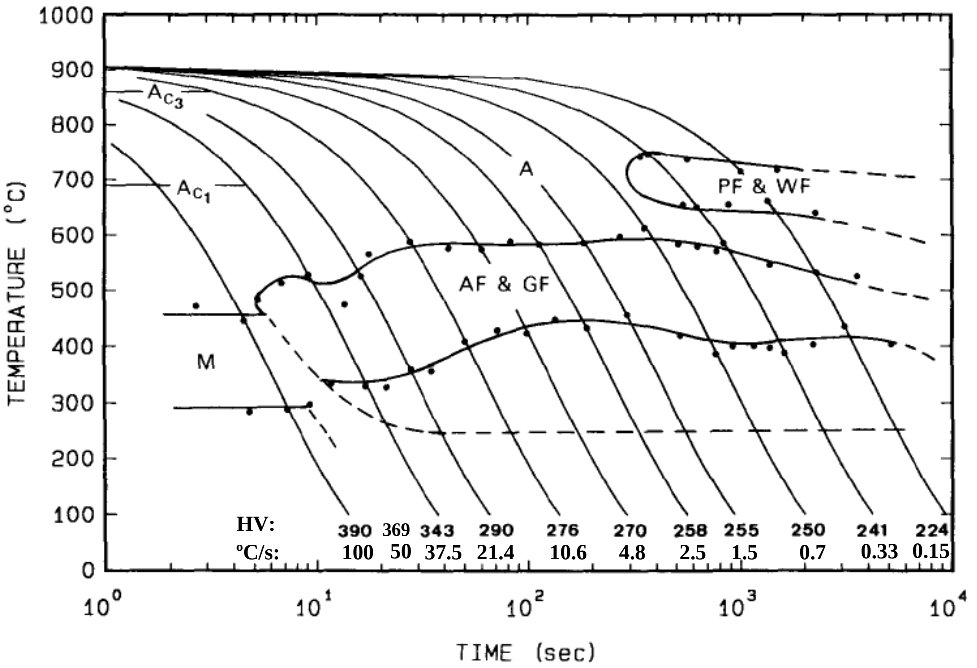

Figure 6.8 - CCT diagram for a HSLA (A: austenite, PF: polygonal ferrite, WF: Widmanstätten ferrite, GF: granular ferrite, AF: acicular ferrite, and M: martensite) [71].

The cooling rates of the samples were within 0.95 and 58 ºC/s and the formation of acicular ferrite was expected by the CCT diagram [71,72].

6.4 Microhardness test results

Figure 6.9 and Figure 6.10 show the distribution of microhardness in four distinct zones (near the substrate, at low mid-section, at high mid-section and near the top surface) on the cross section of the samples P2 and P3 respectively, within a center line along the normal direction and along specimen's width.

Globally for both samples, with the repeatedly reheating and thermal accumulation, the grain size is coarser with the increase of the deposition height, leading to a decrease of the hardness along the parts height.

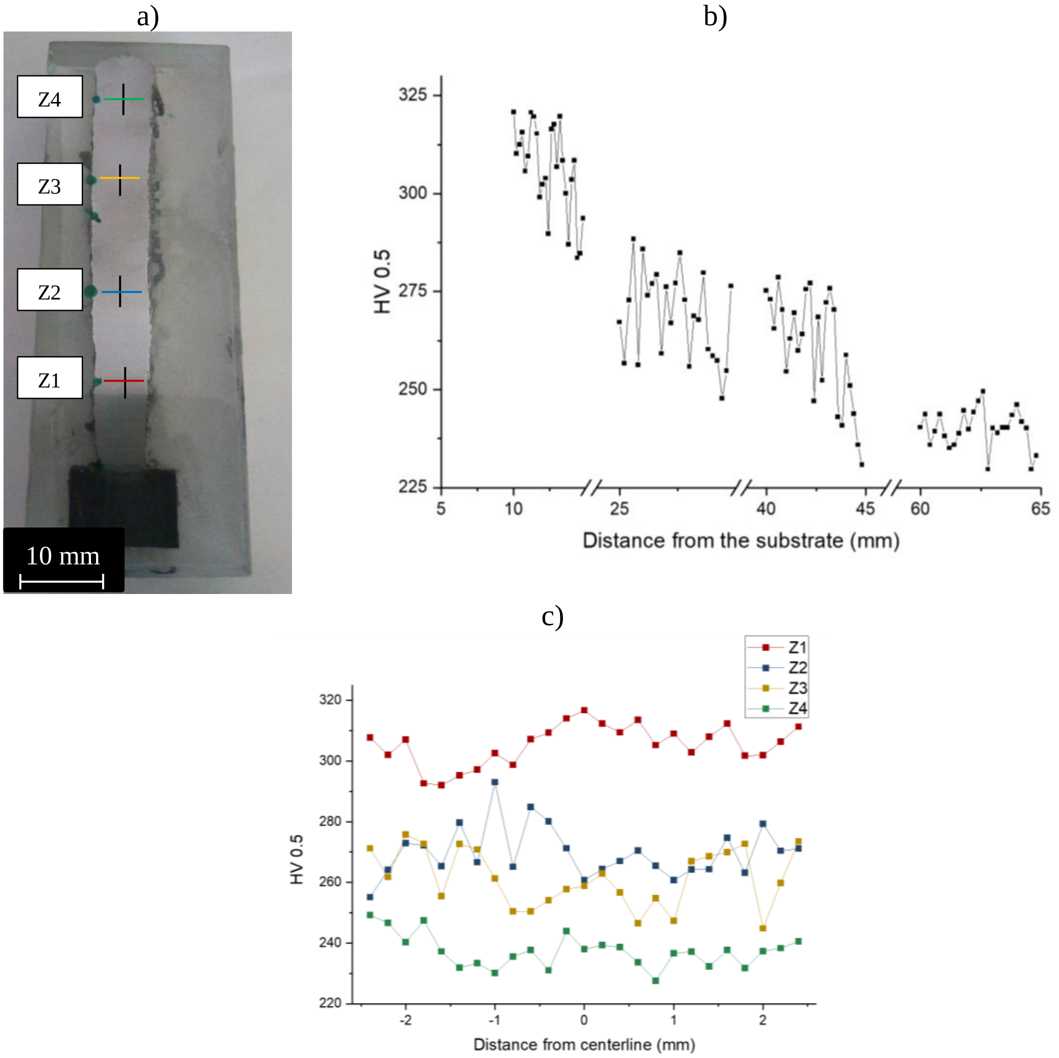

Figure 6.9 - a) Sample P2 cross section, b) Microhardness profiles for sample P2 along the height, c) Microhardness profiles for sample P2 along the width.

In Figure 6.9 it is visible a hardness gradient along the buildup direction for the sample P2. In zone nr. 1 the hardness values are within a range of 283-320 HV, in zone nr. 2 between 247-288 HV, in zone nr. 3 varies amongst 230-278 HV and finally in zone nr. 4 the hardness values varied from 229 HV up to 250 HV.

For the P3 sample that experienced rapid cooling rates resulted in a less evident microhardness gradient along the height. For zone nr. 1 values of hardness between 268-311 HV were measured. For zones 2, 3 and 4 the values were within 268-300, 256-280 and 247-277 HV,respectively.

Overall the microhardness results along the width in each zone were in accordance with the values given by the CCT diagram. Sample P2 experienced cooling rates between from 47.35, down to 0.95 ºC/s, hardness values should be within 369-250 HV, the mean hardness of the regions nr. 1, nr. 2 nr. 3 and nr. 4 along the width was 305, 269 HV, 261 HV and 237 HV respectively. For sample P3 that experienced cooling rates between 58 and 1.3 ºC/s hardness values should be within 369-255 accordingly to the CCT diagram, the mean value for this sample in region nr. 1 was 282 HV and in zone nr. 2 279 HV. Meanwhile, region nr. 3 and nr. 4 registered mean values of 269 HV and 263 HV, respectively.

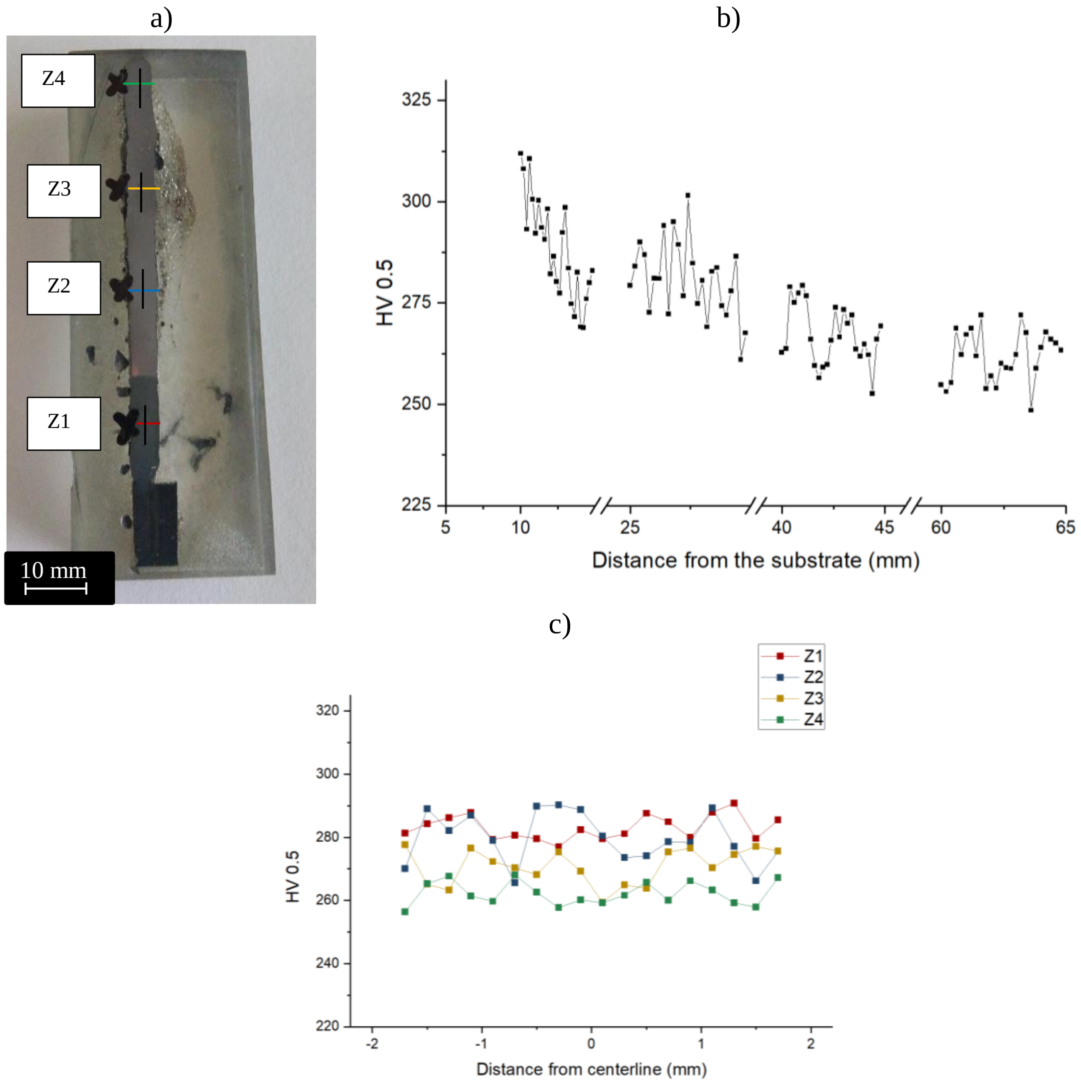

Figure 6.10 - a) Sample P3 cross section, b) Microhardness profiles for sample P3 along the height, c) Microhardness profiles for sample P3 along the width.

The microhardness results suggest the existence of a brittle microstructure near the substrate, however those phases where not distinguished with optical microscopic observations.

6.5 Uniaxial tensile tests

The tensile test results in both longitudinal (Y) and normal (Z) directions are presented in Table 6.7. For comparison, data from welding this electrode provided by the manufacturer is given.

Table 6.7 - Ultimate tensile strenght and elongation to fracture of the tested specimens.

Sample Reference		UTS [MPa] μ ± σ	Elongation to fracture [%] μ ± σ
P1	Y	784 ± 63	n.d.
	Z	809 ± 28	n.d.
P2	Y	755 ± 61	19.50 ± 4.06
	Z	700 ± 28	17.08 ± 1.13
P3	Y	795 ± 7.0	25.62 ± 2.93
	Z	755 ± 35	19.81 ± 1.90
Weld metal [66]		790	22

The results allow to conclude a homogeneity of mechanical proprieties in terms of UTS and elongation between different samples. UTS mean values varies from 700 up to 809 MPa and the elongation from 17.08 up to 25.62 %. The standard deviation of tensile properties along Y direction suggests a homogeneity of mechanical proprieties along the parts height independently of the different cooling rates. Moreover, it is also visible a similar UTS and elongation values between the specimens extracted in the Y and Z directions. Stress-strain curve of P2 specimen removed in both longitudinal (Y) and normal (Z) directions are depicted in Figure 6.11.

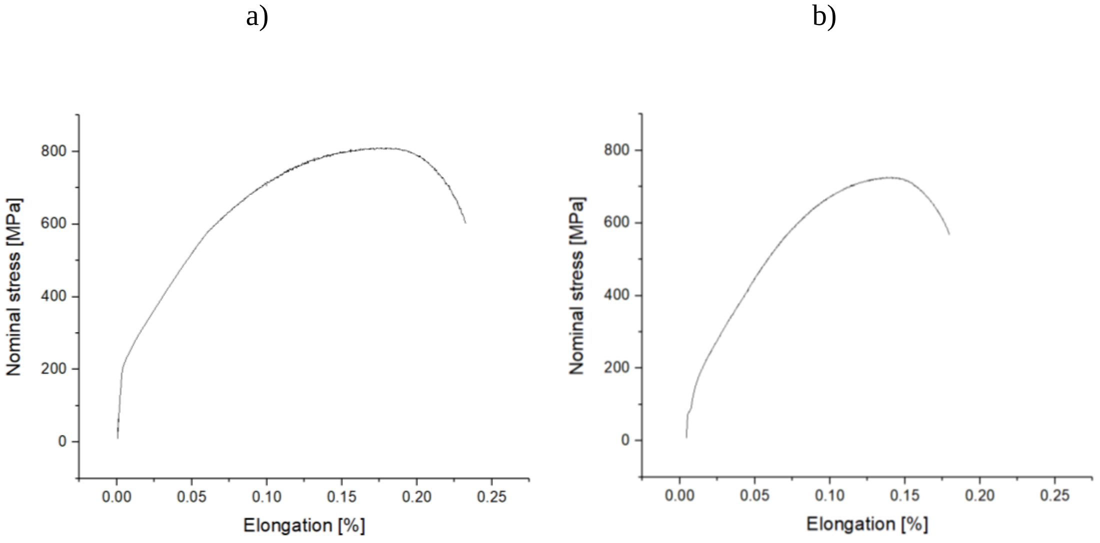

Figure 6.11 - Stress-stain curve of sample P2 in directions: a) longitudinal, b) normal.

6.6 Fractography

The SEM images were acquired from the surface of a longitudinal (Y) P2 with a UTS of 810 MPa and an elongation of 23.2 %. The sample was analyzed in the center of the fracture and near the fracture boundary, results are shown in Figure 6.12. The fractography results displayed consist mainly of dimples, which indicates that the tests specimens experienced a ductile fracture during uniaxial tensile test. The homogeneity of dimples in these two different regions indicates that the fracture was ductile without the existence of transgranular cleavage fractures or other types of fractures.

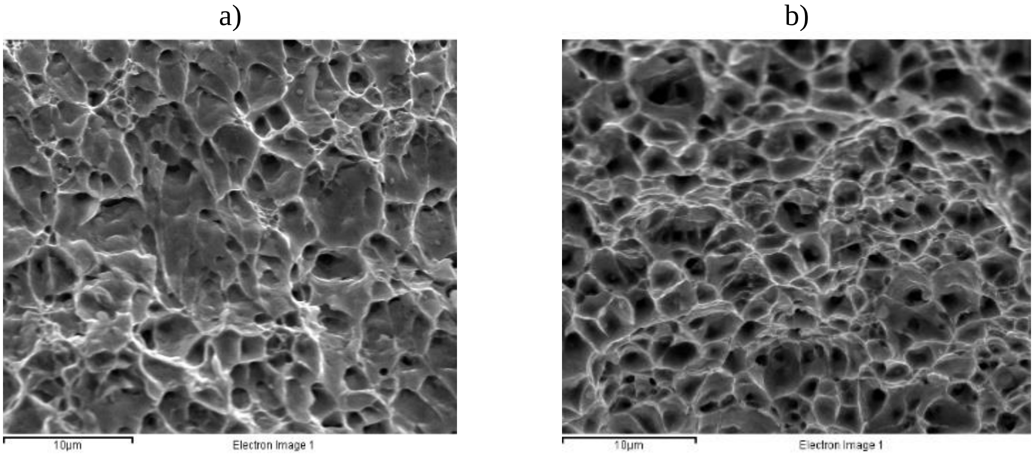

Figure 6.12 - SEM fractographs of a longitudinal P2 tested specimens in: a) center of fracture b) fracture boundary.

6.7 Charpy impact energy test

The results of Charpy impact test from 6 specimens extracted from the part P2, are listed in Table 6.8.

Table 6.8 - Charpy impact test results.

Specimen:		**Toughness [Energy absorbed, J]:**	
		measured	**mean (μ)**
Z	1	18	17.67
	2	18	
	3	17	
Y	1	15	15
	2	15	
	3	15	

The impact toughness of the longitudinal (Y) specimens was of 15 J and for normal (Z) direction samples was 18 J. The difference is within the range of uncertainty of the measurement allowing to conclude that a homogeneity of mechanical proprieties between vertical and horizontal specimens exists, confirming the uniaxial tensile test results.

6.8 Energy-dispersive x-ray spectroscopy

EDS analysis was performed in order to evaluate the chemical composition of the deposited material along the height of the P3 specimen. An area of 10 x 10 µm was analyzed and the results for the different zones are given in Table 6.9.

Table 6.9 - Chemical composition [wt. %] from EDS test.

Element	Z1	Z2	Z3	Z4	Z5
Si	0.29	0.65	0.50	0.54	0.53
Cr	n.a.	0.36	0.36	0.38	0.37
Mn	0.70	1.51	1.46	1.38	1.29
Fe	98.05	96.22	96.25	96.35	96.43
Ni	0.97	1.27	1.44	1.35	1.38

The results shown that the content of the main alloying elements in the wire was maintained and is homogeneous along the wall. The content in Z1 is explained by diffusion of elements from substrate.

6.9 Chapter resume

In this chapter a detailed analysis of the parts manufactured by WAAM is presented. Equipment validation was guaranteed via the fabrication of various parts with optimized process parameters without the existence of internal defects. Cooling rates between two depositions built with different heat input is presented and results are associated with the microscopic observations and with microhardness test results along specimens height. Uniaxial tensile test and Charpy impact test were performed showing isotropic characteristics of the parts produced and with EDS it was shown that there is no detectable loss of alloying elements along the height.

7

Conclusions and suggestions for future work

This thesis aimed to develop and validate an WAAM based manufacturing system of metallic components regardless of their geometry, size and materials. Based on the results achieved the following can be concluded:

1. Concerning equipment performance:
    - A maximum displacement of 0.02 mm was achieved on the accuracy test for the X and Y-axis linear guides. A backlash upon axis turnarounds was observed, which is equal to 0.17 mm. However, this value can be adjust and fed into the software. The verification that this backlash was not incremental during axis turnarounds was further proven by the reproduction of geometry features since the end point was always the same as start. So, an adjustment should only be made if a precisely positioning operation is needed. For the Z-axis linear guides, no deviations were observed with the measurement equipment used;
    - The speed test results demonstrate that for every linear guides, independently of the axis used the experimental data is within acceptable values, confirming system speed accuracy;

  - The displacements resultant of the vibration test was also measured, in which an RMS of 0.06 mm was recorded during bi-directional movement;
  - It was used optimal process parameters to validate the equipment, whose never experienced a technical issue during samples production.
2. Concerning parts manufactured:
  - The specimens manufactured were characterized by isotropic characteristics;
  - The strategy used to mitigate the height variations between the arc start and end positioning was promising. A variation of 3.7 mm was achieved for sample P3;
  - The sample with highest heat input (P2) shown a surface waviness of 355.46 µm;
  - From the comparison of the two different heat input depositions, it was observed that as the height increased the temperature gradient decreases for both depositions. The one with more heat input experienced low cooling rates;
  - In microstructure observations, no cracks or pores were visible;
  - A microstructure mainly of acicular ferrite and perlite was presented in the samples studied, however it was visible a gradient of the grain size along the height;
  - For the P2 sample near the substrate the microhardness test results shown values of 320 HV and near the top surface values of 229 HV;
  - The repeated thermal cycles did not induce a loss of alloying elements along the height;
  - Both uniaxial tensile test and Charpy impact test showed consistent mechanical properties in the longitudinal (Y) and normal (Z) directions specimens.

The equipment is fully operational and to show the potential of this process and mitigate some of its drawbacks some improvements are suggested, such as:

- Study fatigue lifetime of parts manufactured by WAAM;
- Perform a thermal analysis between samples manufactured with an active and inert shielding gas by maintaining equally other process parameters;
- Study other methods to mitigate inconsistent cross section height;
- Install a closed loop system in the equipment to identify defects and control thermal cycles during the process;
- Coupling a mechanism for heating and cooling to control the cooling rate and subsequent microstructure and mechanical proprieties in each region.

References

[1] U.M. Dilberoglu, B. Gharehpapagh, U. Yaman, M. Dolen, The Role of Additive Manufacturing in the Era of Industry 4.0, Procedia Manuf. 11 (2017) 545–554. doi:10.1016/j.promfg.2017.07.148.

[2] Wohlers T, Gornet T (2014) History of additive manufacturing. Wohlers Report. http://wohlersassociates.com/history2014.pdf, (n.d.).

[3] J.P. Oliveira, D. Barbosa, F.M.B. Fernandes, R.M. Miranda, Tungsten inert gas (TIG) welding of Ni-rich NiTi plates: Functional behavior, Smart Mater. Struct. 25 (2016) 03LT01. doi:10.1088/0964-1726/25/3/03LT01.

[4] W.J. Sames, F.A. List, S. Pannala, R.R. Dehoff, S.S. Babu, The metallurgy and processing science of metal additive manufacturing, Int. Mater. Rev. 61 (2016) 315–360. doi:10.1080/09506608.2015.1116649.

[5] ASTM F2792-12a, Standard Terminology for Additive Manufacturing Technologies, (Withdrawn 2015), ASTM International, West Conshohocken, PA, 2012, n.d.

[6] I. Gibson, D.W. Rosen, B. Stucker, Additive Manufacturing Technologies: Rapid Prototyping to Direct Digital Manufacturing, Media. (2010) 193–198. doi:10.1595/205651315X688406.

[7] K. V. Wong, A. Hernandez, A Review of Additive Manufacturing, ISRN Mech. Eng. 2012 (2012) 1–10. doi:10.5402/2012/208760.

[8] P.M.S. ALMEIDA, Process Control and Development in Wire and Arc Additive Manufacturing, (2012) 1–467.

[9] F. Zezulka, P. Marcon, I. Vesely, O. Sajdl, Industry 4.0 – An Introduction in the phenomenon, IFAC-PapersOnLine. 49 (2016) 8–12. doi:10.1016/j.ifacol.2016.12.002.

[10] S. Williams and F. Martina, ‘Wire + arc additive manufacturing vs. traditional machining from solid: a cost comparison’, http://waammat.com/documents/waam-vs-machining-from-solid-a-cost- comparison, April 2015.

[11] T. DebRoy, H.L. Wei, J.S. Zuback, T. Mukherjee, J.W. Elmer, J.O. Milewski, A.M. Beese, A. Wilson-Heid, A. De, W. Zhang, Additive manufacturing of metallic components –

Process, structure and properties, Prog. Mater. Sci. 92 (2018) 112–224. doi:10.1016/j.pmatsci.2017.10.001.

[12] J. Steen, William, Mazumder, Laser Material Processing, 2010.

[13] S.A.M. Tofail, E.P. Koumoulos, A. Bandyopadhyay, S. Bose, L. O'Donoghue, C. Charitidis, Additive manufacturing: Scientific and technological challenges, market uptake and opportunities, Mater. Today. 00 (2017) 1–16. doi:10.1016/j.mattod.2017.07.001.

[14] Atwood, C & Ensz, M & Greene, D & Griffith, M & Harwell, L & Reckaway, D & Romero, T & Schlienger, E & Smugeresky, J. (1998). Laser Engineered Net Shaping (LENS(TM)): A Tool for Direct Fabrication of Metal Parts. ., (n.d.).

[15] R.M. Miranda, G. Lopes, L. Quintino, J.P. Rodrigues, S. Williams, Rapid prototyping with high power fiber lasers, Mater. Des. 29 (2008) 2072–2075. doi:10.1016/j.matdes.2008.03.030.

[16] D. Ding, Z. Pan, D. Cuiuri, H. Li, Wire-feed additive manufacturing of metal components: technologies, developments and future interests, Int. J. Adv. Manuf. Technol. 81 (2015) 465–481. doi:10.1007/s00170-015-7077-3.

[17] P. Kazanas, P. Deherkar, P. Almeida, H. Lockett, S. Williams, Fabrication of geometrical features using wire and arc additive manufacture, Proc. Inst. Mech. Eng. Part B J. Eng. Manuf. 226 (2012) 1042–1051. doi:10.1177/0954405412437126.

[18] J. Xiong, Y. Lei, H. Chen, G. Zhang, Fabrication of inclined thin-walled parts in multi-layer single-pass GMAW-based additive manufacturing with flat position deposition, J. Mater. Process. Technol. 240 (2017) 397–403. doi:10.1016/j.jmatprotec.2016.10.019.

[19] T.M. Mower, M.J. Long, Mechanical behavior of additive manufactured, powder-bed laser-fused materials, Mater. Sci. Eng. A. 651 (2016) 198–213. doi:10.1016/j.msea.2015.10.068.

[20] V. Bhavar, P. Kattire, P. Pawar, S. Khot, K. Gujar, R. Singh, A Review on Powder Bed Fusion Technology of Additive Manufacturing, Process. Appl. Perform. Mater. Addit. Manuf. (2014).

[21] M. Jamshidinia, A. Sadek, W. Wang, S. Kelly, Additive manufacturing: Of steel alloys using laser powder-bed fusion, Adv. Mater. Process. 173 (2015) 20–24.

doi:10.1007/s11837-014-1273-8.

[22] C. Kamath, G.F. Gallegos, A. Sisto, Density of Additively-Manufactured , 316L SS Parts Using Laser Powder-Bed Fusion at Powers Up to 400W, (2013). doi:10.2172/1116929.

[23] T.T. Qian, D. Liu, X.J. Tian, C.M. Liu, H.M. Wang, Microstructure of TA2/TA15 graded structural material by laser additive manufacturing process, Trans. Nonferrous Met. Soc. China (English Ed. 24 (2014) 2729–2736. doi:10.1016/S1003-6326(14)63404-X.

[24] http://www.arcam.com/wp-content/uploads/arcamebm-corp-brochure-fnlv3.pdf, (n.d.).

[25] H.K. Rafi, N. V. Karthik, H. Gong, T.L. Starr, B.E. Stucker, Microstructures and mechanical properties of Ti6Al4V parts fabricated by selective laser melting and electron beam melting, J. Mater. Eng. Perform. 22 (2013) 3872–3883. doi:10.1007/s11665-013-0658-0.

[26] H.P. Tang, M. Qian, N. Liu, X.Z. Zhang, G.Y. Yang, J. Wang, Effect of Powder Reuse Times on Additive Manufacturing of Ti-6Al-4V by Selective Electron Beam Melting, Jom. 67 (2015) 555–563. doi:10.1007/s11837-015-1300-4.

[27] A. Strondl, M. Palm, J. Gnauk, G. Frommeyer, Microstructure and mechanical properties of nickel based superalloy IN718 produced by rapid prototyping with electron beam melting (EBM), Mater. Sci. Technol. 27 (2011) 876–883. doi:10.1179/026708309X12468927349451.

[28] G.K. Lewis, E. Schlienger, Practical considerations and capabilities for laser assisted direct metal deposition, Mater. Des. 21 (2000) 417–423. doi:10.1016/S0261-3069(99)00078-3.

[29] J.S. Keist, T.A. Palmer, Role of geometry on properties of additively manufactured Ti-6Al-4V structures fabricated using laser based directed energy deposition, Mater. Des. 106 (2016) 482–494. doi:10.1016/j.matdes.2016.05.045.

[30] J. Alcisto, A. Enriquez, H. Garcia, S. Hinkson, T. Steelman, E. Silverman, P. Valdovino, H. Gigerenzer, J. Foyos, J. Ogren, J. Dorey, K. Karg, T. McDonald, O.S. Es-Said, Tensile properties and microstructures of laser-formed Ti-6Al-4V, J. Mater. Eng. Perform. 20 (2011) 203–212. doi:10.1007/s11665-010-9670-9.

[31] G.P. Dinda, L. Song, J. Mazumder, Fabrication of Ti-6Al-4V scaffolds by direct metal deposition, Metall. Mater. Trans. A Phys. Metall. Mater. Sci. 39 (2008) 2914–2922.

doi:10.1007/s11661-008-9634-y.

[32] K. Malukhin, K. Ehmann, Material Characterization of NiTi Based Memory Alloys Fabricated by the Laser Direct Metal Deposition Process, J. Manuf. Sci. Eng. 128 (2006) 691. doi:10.1115/1.2193553.

[33] M. Ma, Z. Wang, X. Zeng, Effect of energy input on microstructural evolution of direct laser fabricated IN718 alloy, Mater. Charact. 106 (2015) 420–427. doi:10.1016/j.matchar.2015.06.027.

[34] M.K. Imran, S.H. Masood, M. Brandt, S. Bhattacharya, J. Mazumder, Direct metal deposition (DMD) of H13 tool steel on copper alloy substrate: Evaluation of mechanical properties, Mater. Sci. Eng. A. 528 (2011) 3342–3349. doi:10.1016/j.msea.2010.12.099.

[35] D. Herzog, V. Seyda, E. Wycisk, C. Emmelmann, Additive manufacturing of metals, Acta Mater. 117 (2016) 371–392. doi:10.1016/j.actamat.2016.07.019.

[36] S. Liu, W. Liu, M. Harooni, J. Ma, R. Kovacevic, Real-time monitoring of laser hot-wire cladding of Inconel 625, Opt. Laser Technol. 62 (2014) 124–134. doi:10.1016/j.optlastec.2014.03.007.

[37] E. Brandl, B. Baufeld, C. Leyens, R. Gault, Additive manufactured Ti-6A1-4V using welding wire: Comparison of laser and arc beam deposition and evaluation with respect to aerospace material specifications, Phys. Procedia. 5 (2010) 595–606. doi:10.1016/j.phpro.2010.08.087.

[38] B. Baufeld, E. Brandl, O. Van Der Biest, Wire based additive layer manufacturing: Comparison of microstructure and mechanical properties of Ti-6Al-4V components fabricated by laser-beam deposition and shaped metal deposition, J. Mater. Process. Technol. 211 (2011) 1146–1158. doi:10.1016/j.jmatprotec.2011.01.018.

[39] S.W. Williams, F. Martina, A.C. Addison, J. Ding, G. Pardal, P. Colegrove, Wire + Arc Additive Manufacturing, Mater. Sci. Technol. 32 (2016) 641–647. doi:10.1179/1743284715Y.0000000073.

[40] D. Ding, Z. Pan, S. van Duin, H. Li, C. Shen, Fabricating superior NiAl bronze components through wire arc additive manufacturing, Materials (Basel). 9 (2016). doi:10.3390/ma9080652.

[41] V.R. Duarte, Additive manufacturing of a high resistance steel by MIG / MAG, (2016).

[42] H. Geng, J. Li, J. Xiong, X. Lin, Optimisation of interpass temperature and heat input for wire and arc additive manufacturing 5A06 aluminium alloy, Sci. Technol. Weld. Join. 22 (2017) 472–483. doi:10.1080/13621718.2016.1259031.

[43] Z. Hu, X. Qin, T. Shao, Welding Thermal Simulation and Metallurgical Characteristics Analysis in WAAM for 5CrNiMo Hot Forging Die Remanufacturing, Procedia Eng. 207 (2017) 2203–2208. doi:10.1016/j.proeng.2017.10.982.

[44] C.L. Jenney, A. O'Brien, Welding handbook-II part I, 1991.

[45] https://www.oerlikon-welding.com/processes/mig-mag-welding-process, (n.d.).

[46] D. Iordachescu, L. Quintino, R. Miranda, G. Pimenta, Influence of shielding gases and process parameters on metal transfer and bead shape in MIG brazed joints of the thin zinc coated steel plates, Mater. Des. 27 (2006) 381–390. doi:10.1016/j.matdes.2004.11.010.

[47] E. Ab, Rohde H, Katic J, Paschold R. (ESAB GmbH, Solingen), ESAB pulsed gas-shielded metal arc brazing of surface-coated sheets.Svetsaren 2000;3:20–23, (n.d.).

[48] Kersche, A., Trube, S. (Linde AG, Linde Gas Division, Hoellriegelskreuth), Shielding Gases for Gas-shielded Metal Arc Brazing, Lecture at "Thin Sheet Metal Conference", SLV Munich on 28th March 2000, Special edition, Nr. 50/02, (n.d.).

[49] P. Almeida, S. Williams, Innovative process model of Ti–6Al–4V additive layer manufacturing using cold metal transfer (CMT), Solid Free. Fabr. Symp. (2010) 25–36.

[50] B. Ralph, Method of making decorative articles,US 1533300 A, n.d.

[51] N.P. O, Method and apparatus for electric arc welding,US 1898060 A, 1933.

[52] B.H.K. Clyde O. Brown, Edward M. Breinan, Method for fabricating articles by sequential layer deposition US 4323756 A, 1982.

[53] F. Ribeiro, B. Ogunbiyi, J. Norrish, Mathematical model of welding parameters for rapid prototyping using robot welding, Sci. Technol. Weld. Join. 2 (1997) 185–190. doi:10.1179/136217197791069984.

[54] J. Xiong, G. Zhang, H. Gao, L. Wu, Modeling of bead section profile and overlapping beads with experimental validation for robotic GMAW-based rapid manufacturing, Robot. Comput. Integr. Manuf. 29 (2013) 417–423. doi:10.1016/j.rcim.2012.09.011.

[55] V.R. Duarte, Additive manufacturing of a high resistance steel by MIG/MAG, Faculdade

de Ciências e Tecnologia e Universidade Nova de Lisboa, 2016.

[56] X. Xu, J. Ding, S. Ganguly, C. Diao, S. Williams, Oxide accumulation effects on wire + arc layer-by-layer additive manufacture process, J. Mater. Process. Technol. 252 (2018) 739–750. doi:10.1016/j.jmatprotec.2017.10.030.

[57] J. Ding, P. Colegrove, F. Martina, S. Williams, R. Wiktorowicz, M.R. Palt, Development of a laminar flow local shielding device for wire + arc additive manufacture, J. Mater. Process. Technol. 226 (2015) 99–105. doi:10.1016/j.jmatprotec.2015.07.005.

[58] P.J. Withers, H.K.D.H. Bhadeshia, Residual stress. Part 1–measurement techniques, Mater. Sci. Technol. 17 (2001) 355–365. doi:10.1179/026708301101509980.

[59] M.P. Mughal, H. Fawad, R.A. Mufti, M. Siddique, Deformation modelling in layered manufacturing of metallic parts using gas metal arc welding: Effect of process parameters, Model. Simul. Mater. Sci. Eng. 13 (2005) 1187–1204. doi:10.1088/0965-0393/13/7/013.

[60] P.A. Colegrove, H.E. Coules, J. Fairman, F. Martina, T. Kashoob, H. Mamash, L.D. Cozzolino, Microstructure and residual stress improvement in wire and arc additively manufactured parts through high-pressure rolling, J. Mater. Process. Technol. 213 (2013) 1782–1791. doi:10.1016/j.jmatprotec.2013.04.012.

[61] J. Xiong, Y. Lei, R. Li, Finite element analysis and experimental validation of thermal behavior for thin-walled parts in GMAW-based additive manufacturing with various substrate preheating temperatures, Appl. Therm. Eng. 126 (2017) 43–52. doi:10.1016/j.applthermaleng.2017.07.168.

[62] D. Ding, Z. Pan, D. Cuiuri, H. Li, A multi-bead overlapping model for robotic wire and arc additive manufacturing (WAAM), Robot. Comput. Integr. Manuf. 31 (2015) 101–110. doi:10.1016/j.rcim.2014.08.008.

[63] Y. Nilsiam, P. Sanders, J.M. Pearce, Slicer and process improvements for open-source GMAW-based metal 3-D printing, Addit. Manuf. 18 (2017) 110–120. doi:10.1016/j.addma.2017.10.007.

[64] J. L, J.L. Diéguez, A. Santana, P. Afonso, A. Zanin, R. Wernke, Preliminary development of a Wire and Arc Additive Manufacturing system (WAAM) Manufacturing system (WAAM) Costing models capacity optimization Industry Trade-off between used capacity operational efficiency Nacional and Preliminary development of a W, Procedia Manuf. 13 (2017) 895–902. doi:10.1016/j.promfg.2017.09.154.

[65] J. Xiong, Z. Yin, W. Zhang, Closed-loop control of variable layer width for thin-walled parts in wire and arc additive manufacturing, J. Mater. Process. Technol. 233 (2016) 100–106. doi:10.1016/j.jmatprotec.2016.02.021.

[66] The Lincoln Electric Company, “ LNM MoNiVa ER110S-G consumable electrode technical data,” n.d.

[67] D. Yang, G. Wang, G. Zhang, Thermal analysis for single-pass multi-layer GMAW based additive manufacturing using infrared thermography, J. Mater. Process. Technol. 244 (2017) 215–224. doi:10.1016/j.jmatprotec.2017.01.024.

[68] Y.M. Zhang, Y. Chen, P. Li, A.T. Male, Weld deposition-based rapid prototyping: A preliminary study, J. Mater. Process. Technol. 135 (2003) 347–357. doi:10.1016/S0924-0136(02)00867-1.

[69] AWS Welding Handbook - Metals and Their Weldability - Vol 4 - 7th Edition, n.d.

[70] E.M.D.L. and R.M. Miranda, Metalurgia da soldadura, Lisboa, 1993.

[71] S.W. Thompson, D.J. Vin Col, G. Krauss, Continuous cooling transformations and microstructures in a low-carbon, high-strength low-alloy plate steel, Metall. Trans. A. 21 (1990) 1493–1507. doi:10.1007/BF02672564.

[72] Y. Shao, C. Liu, Z. Yan, H. Li, Y. Liu, Formation mechanism and control methods of acicular ferrite in HSLA steels: A review, J. Mater. Sci. Technol. 34 (2018) 737–744. doi:10.1016/j.jmst.2017.11.020.